



Multi-field coupling multiple nonlinear vibration model and fatigue failure mechanism of deep-ocean mining hydraulic lifting pipe

Xiaoqiang Guo · Xinghan Chen · Libin Zhao · Xinye Li

Received: 7 April 2023 / Accepted: 6 July 2023 / Published online: 20 July 2023
© The Author(s), under exclusive licence to Springer Nature B.V. 2023

Abstract In deep-ocean mining operation, the fatigue life of lifting pipe has always been the focus of field operators, and the fatigue failure mechanism has attracted more and more attention of scholars, but it has not been effectively disclosed. Therefore, in this work, a multi-field coupling and multiple nonlinear vibration model of lifting pipe is established, which can accurately determine the alternating stress of deep-ocean lifting pipe. The nonlinear fatigue damage prediction method of lifting pipe based on load interaction effect and residual strength attenuation degradation is established using Corten–Dolan cumulative damage method, which can accurately determine the fatigue life of deep-ocean lifting pipe. Finally, the influences of outflow velocity, buffer station masses and internal flow velocity on the fatigue life of lifting pipe are analyzed. It is found that, firstly, with the increase in the outflow velocity, the fatigue life of the pipe tends to decrease first and then increase, and an external flow rate with the maximum fatigue life appears. However, in real operation, the external flow rate cannot be controlled. Therefore, according to

a certain external flow rate, the optimal structure setting can be evaluated by the analysis method established. Secondly, with the increase in the buffer station mass, the fatigue life of the lifting pipe tends to decrease first and then increase. There is an optimal buffer station mass configuration parameter on the site, which is related to the riser structure, ocean flow velocity, internal flow velocity and can be determined by the analysis methodology. Thirdly, with the increase in the lifting flow rate, the fatigue life of the lifting pipe tends to increase first and then decrease. Therefore, when determining to configure the lifting flow rate on-site, it is necessary to use the proposed nonlinear fatigue damage analysis methodology to analyze whether it is in a dangerous state. If it does not meet the site requirements, other parameters can be set, to improve the fatigue life of the lifting pipe.

Keywords Pipe string mechanics · Hydraulic lifting pipe · Multi-field coupling · Multiple nonlinear vibration · Failure mechanism

Abbreviations

VIV	Vortex-induced vibration
CF	Cross flow
RMS	Root mean square
CFD	Computational fluid dynamics
IL	In-line
3D	Three-dimensional

X. Guo (✉) · X. Chen · L. Zhao · X. Li
School of Mechanical Engineering, Hebei University of
Technology, Tianjin 300401, China
e-mail: 786526101@qq.com

X. Guo
Key Laboratory of Gas Hydrate, Guangzhou Institute of
Energy Conversion, Chinese Academy of Sciences,
Guangzhou 510640, China

List of symbols

$u_1(z, t)$	Displacement field function corresponding to coordinate system x	$\hat{\omega}_i$	Circular frequency of the i -th harmonic
$u_3(z, t)$	Displacement field function corresponding to coordinate system z	M	Interval number of the partition
$v_y(z, t)$	CF displacement of lifting pipe	$\Delta\omega$	Frequency step
E	Elastic modulus of the lifting pipe material	\bar{f}	The frequency
L	Length of the lifting pipe unit	$H_{1/3}$	Significant wave height
$v''_i, i = x, y, z$	Second derivative of the lifting pipe displacements with respect to z	f_p	Peak frequency
v_x, v_y, v_z	Absolute velocities of the internal fluid in the x -, y - and z -directions	γ	Peak parameter
ρ_i	Internal fluid density	R	Platform radius
$\dot{v}_i, i = x, y, z$	First-order derivative of the lifting pipe displacement with respect to time for the x -, y - and z -directions	d	Draft of the platform
U	Multiphase flow velocity in the lifting pipe unit	B_{plate}	Width of the heave plate
$F_L(z, t)$	Lateral lift in the CF direction	p	Number of damage nuclei under stress
$f_y(z, t)$	High-speed fluid impact loads in the lifting pipe in the y -directions	a	Constant related to the material
$F_x(z, t)$	Longitudinal force of the lifting pipe	p_{max}	Number of damage nuclei
$\alpha_1(t)$	Deflection angles of the upper micro-segments in the x -directions	a_{max}	Material constant
$\varphi_1(t)$	Deflection angles of the lower micro-segments in the y -directions	p_i	Number of damage nuclei
ζ	Damping ratio	a_i	Material constant
D_o	Outer diameter of the lifting pipe	N_f	Fatigue life under multistage stress cycle
f	Friction coefficient caused by fluid viscosity	σ_i	The i stress
c	Damping coefficient	d	Parameter related to material properties
M_C	Mass of the buffer station	$R(n)$	Material residual strength
\bar{C}_d, \bar{C}_l	Steady-state drag force coefficient and lift force coefficient	A_i	Strength degradation coefficient
q_x, q_y	Dimensionless wake oscillator variables in the IL flow direction and CF direction	$u_2(z, t)$	Displacement field function corresponding to coordinate system y
S_f	Strouhal coefficient	$v_x(z, t)$	IL displacement of lifting pipe
d_p	Element generalized force matrix	$v_z(z, t)$	Longitudinal displacement of lifting pipe
C_p	Particle drag force coefficient	A	Cross-sectional area of the lifting pipe
P	Internal pressure	$v'_i, i = x, y, z$	First-order derivative of the lifting pipe displacements with respect to z
τ_i	Fluid viscous shear stress	A_i	Internal cross-sectional area of the lifting pipe
λ_m	Wall friction coefficient	$\dot{u}_i, i = 1, 2, 3$	First-order derivative of lifting pipe displacements function with respect to time for coordinate system x, y, z
B_1, B_2	Heave radiation and heave viscous damping	m_v	Mass of lifting pipe unit length
$\eta(t)$	Surface displacements of the random wave	m_i	Mass of the multiphase flow velocity in the lifting pipe unit
		$F_D(z, t)$	Drag force in the IL direction
		$f_x(z, t)$	High-speed fluid impact loads in the lifting pipe in the x -direction
		$f_z(z, t)$	High-speed fluid impact loads in the lifting pipe in the z -directions
		W_f	Fluid viscous damping
		$\alpha_2(t)$	Deflection angles of the lower micro-segments in the x -directions

$\varphi_2(t)$	Deflection angles of the lower micro-segments in the y -directions
ρ_w	Density of seawater
D_i	Inner diameter of the lifting pipe
m_a	Additional mass per unit length of pipe string
$u_{\text{boat}}(t)$	Platform heave displacement
U_c	External flow velocity of lifting pipe
C'_d, C'_l	Reference drag force coefficient and reference lift force coefficient
ω_s	Shedding frequency of wake vortex
$\varepsilon_x, \varepsilon_y, A_x, A_y$	Dimensionless parameters
ρ_s	Density of solid particles
ΔV	Selected control volume
α	Inclination angle of pipe string
τ_m	Wall shear stress
m_p	Mass of the platform
A_w	Area of the platform at sea level
\bar{F}_z	Random heave wave exciting force on the platform
\bar{e}_i	Initial phase of the i -th harmonic component
a_i	Amplitude of the i -th harmonic component
$S(\omega)$	Random wave spectrum
ω	The circular frequency
$T_{1/3}$	Significant period
T_p	Peak period
σ	Peak shape coefficient
k	Wave number
z_{plate}	Depth of heave plate
D	Fatigue cumulative damage
r	Damage coefficient
D_c	Critical fatigue damage
r_{max}	Component forces of the transverse damage coefficient
N_{max}	Number of cycles under the action of maximum stress
r_i	Damage coefficient
n_i	Number of cycles
a_i	Percentage for the number
σ_{max}	Maximum stress in multistage stress
N_{fi}	Fatigue life under action of the single σ_i stress
p', q	Material constants
A_0	Strength degradation coefficient

1 Introduction

The deep-ocean contains rich mineral resources with various types, large reserves and high grade, which has huge development and utilization prospects and has become an important strategic development goal for all countries in the world [1, 2]. Currently, hydraulic lifting technology is one of the most effective technologies for obtaining deep-ocean metal minerals and has been attracting the attention of scholars and companies in our world [3]. Among them, riser is the only channel connecting the seabed and mining vessels, playing a connecting role, and its safety has also received attention from scholars (as shown in Fig. 1) [4]. During the operation, the riser is subjected to external ocean current vortex-induced effects, action of internal liquid–solid two-phase flow and the heave motion of the platform, making it extremely prone to nonlinear vibration and inducing its fatigue failure. Therefore, it is urgent to establish a multi-field coupled multiple nonlinear vibration model and fatigue life prediction model for deep-ocean mining hydraulic riser, and explore its fatigue failure mechanism.

Early scholars mainly studied the vortex-induced vibration (VIV) vibration of riser. At that time, offshore oil and gas production was in shallow water, and the riser was regarded as a rigid structure as the research object [5, 6], and the frequency-locked phenomenon [7] and lagging behavior [8] were obtained. With the increase in water depth, the length

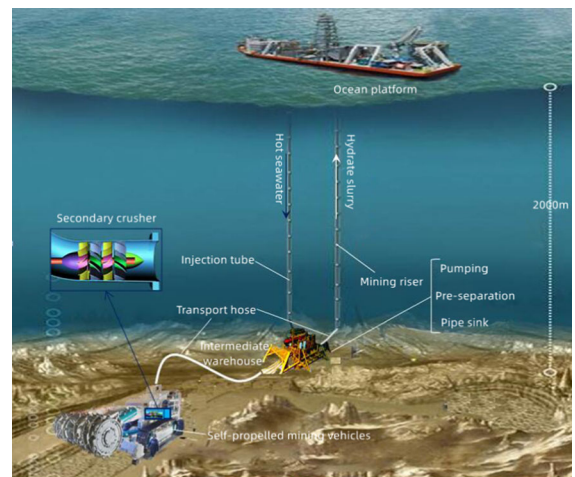


Fig. 1 Schematic diagram of mechanical analysis of lifting pipe in deep-ocean mining

of the riser also increases, and its aspect ratio (the ratio of length to diameter) also increases. It is unreasonable to regard the riser as a rigid structure. Therefore, some scholars regard it as a flexible structure. Physical experiments [9, 10] and computational fluid dynamics (CFD) numerical simulations [11, 12] are the two most common methods in these studies. At the beginning, scholars mainly studied the vibration in one direction of the deep-sea riser, that is, the cross-flow (CF) direction. Mathelin and Langre [13] regarded marine fluid as shear flow and explored the vibration response of riser. Moreover, Xu et al. [14] and He et al. [15] studied the effects of the flow velocity, top tension and pipe diameter on VIV behavior of a riser, and the optimization method of field operation parameters and structural parameters is put forward. However, Jauvtis and Williamson [16] found that as the mass ratio, the ratio of the structural quality to the mass of discharged fluid was less than 6.0, and the in-line (IL) vibration of a cylinder could not be neglected. The VIV characteristics study of a rigid cylinder presented by Gu et al. [17], Martins et al. [18] and Gao et al. [19]. In our recent work [20, 21], the response characteristics of VIV of marine risers with consideration of the coupling effects of the CF and IL vibration were investigated. It is found that the vibration amplitude in the downstream direction is twice that in the transverse direction, but the vibration frequency in the downstream direction is only half of that in the transverse direction. However, the existing VIV vibration research of deep-water riser ignores the influence of internal pipe string, and the on-site deep-water riser is a typical pipe in pipe structure, resulting in the prediction accuracy of the current vibration analysis model is different from that of the on-site. To solve this problem, the author established a three-dimensional nonlinear vibration model of deep-water riser test pipe in our previous research [22], which laid a foundation for the vibration analysis model of this paper.

The above studies have laid a methodological foundation for the establishment of nonlinear vibration model of deep-sea hydraulic riser. However, the biggest difference between deep-sea hydraulic riser and deep-sea oil and gas production riser is that the former has a single fluid in the pipe, while the latter has

a liquid–solid multiphase flow in the pipe, resulting in the difference of vibration characteristics between the two risers. Scholar has established a horizontal pipeline gas–liquid two-phase flow-induced vibration model to address the problem of two-phase flow-induced vibration in rigid pipelines [23] and found that pipeline vibration response is closely related to two-phase flow parameters (density, pressure and flow velocity). With the improvement of experimental instrument performance and the development of computer technology, some scholars have adopted theoretical methods combined with numerical simulation technology to establish gas–liquid two-phase flow-induced vibration models for steam generator heat transfer tubes [24] and gas–liquid two-phase flow-induced vibration models for marine flexible risers [25]. Zhu et al. used experimental methods to investigate the vibration caused by gas–liquid two-phase flow in marine flexible risers and found that the gas–liquid ratio and gas–liquid two-phase flow velocity are the main factors affecting the vibration of flexible risers [26]. Liu has studied the problem of solid–liquid two-phase flow-induced vibration in deep-sea lifting pipes, established a particle flow model inside the pipe and a solid–liquid two-phase flow-induced vibration model in the lifting pipe and found that particle concentration and transport speed are the main influencing factors on the vibration response of the lifting pipe [27]. With the deepening of research, it has been found that internal flow has the greatest impact on the vibration characteristics of the lifting pipe. However, the impact of steady-state internal flow on the vibration characteristics of the riser has been the focus of some scholars' attention, and corresponding research has been carried out [28, 29], and found that the vibration frequency and displacement of the lifting pipe are most sensitive to the influence of internal flow velocity and density. The change of internal flow velocity and density will trigger the new vibration modal response of the flexible riser. Some scholars used the finite element method [30] and the finite element software ADINA [31] to study the influence of unsteady pulp flow on the dynamic characteristics of the lifting pipe and found that the solid content has a significant impact on the natural frequency of the lifting pipe. The internal

multiphase flow has an important influence on the vibration of the opposite pipe. With the increase in transport concentration and transport speed, the stress and displacement increase. Some researchers have investigated the influence of mine lifting pipe vibration on the internal flow in the pipe. For example, Liu et al. [32] used the Euler two fluid models based on particle dynamics and computational fluid dynamics (CFD) technology to simulate the solid–liquid two-phase flow in the pipeline under vortex-induced vibration and found that under the action of vortex-induced vibration, the axial velocity distribution of particles fluctuated, and the particle concentration distribution changed periodically. Yoon et al. [33] studied the interaction between the movement of the 5000-m deep-sea mining lifting pipe and the internal flow of the hard pipe with the finite element method and found that the movement of the lifting pipe has relatively little effect on the internal flow.

At present, the research on deep-sea hydraulic riser mainly focuses on the vibration model and vibration characteristics and lacks the fatigue failure mechanism caused by vibration. However, the fatigue failure mechanism of deep-sea riser mainly focuses on the oil and gas well production riser. Some scholars have established the fatigue life prediction method of riser using different methods, including the fatigue life prediction model [34, 35], the crack propagation model [36] and the fatigue reliability analysis model [37]. Aiming at the fatigue failure mechanism of deep-water riser, Lekkala et al. [38] optimized the existing excitation coefficient database to improve the fatigue damage prediction of riser attached with staggered buoyancy modules, which reduce the error in the predicting the VIV response of the riser with staggered buoyancy modules. In order to the problem of fatigue failure of risers caused by slug flow, Jeong et al. [39] have established an in-house program to calculate local stress and fatigue damage of risers, exploring the influence of riser materials, riser structure, internal flow velocity and environmental factors on the fatigue life of risers. Some scholars have established corresponding dynamic models and fatigue prediction methods for the vibration fatigue damage of marine risers under special working conditions, exploring the fatigue damage laws of risers under different operating

and structural parameters and ultimately revealing the fatigue damage mechanism of risers under special working conditions Ruan et al. [40] and Gao et al. [41].

Above all, in this paper, a vibration model with multi-field coupling and multiple nonlinearity of mining lifting pipe is established using the finite element method and Hamilton variational principle, which not only considers the multi-field coupling effect between the ocean flow field, the riser stress field and the internal flow field, but also considers the vertical and horizontal coupling nonlinearity of the riser, the vortex-induced nonlinearity of the ocean load and the flow-induced nonlinearity of the internal flow field. Based on finite element theory, the numerical solution of the nonlinear vibration model is realized. The correctness of the model is verified by comparing the calculated results of the theoretical model with the test results of the simulation experiment. Then, the nonlinear fatigue damage prediction method of deep-water lifting pipe based on load interaction effect and residual strength attenuation degradation is established using Corten–Dolan cumulative damage method, which can accurately determine the fatigue life of deep-ocean lifting pipe. Finally, the influences of structural parameters and operation parameters on the fatigue life of deep-ocean lifting pipe are explored, which lays a theoretical foundation for the parameter design of deep-ocean lifting pipe on-site.

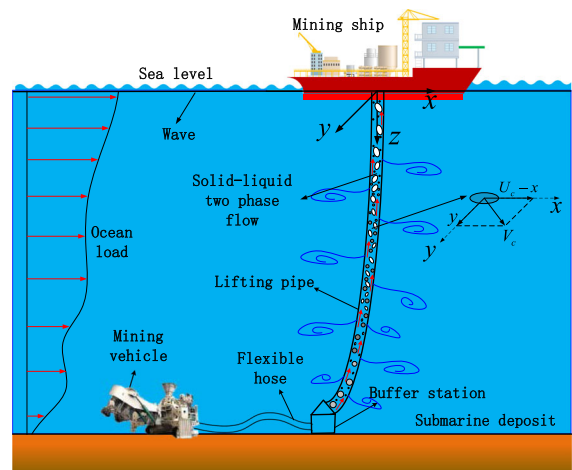


Fig. 2 Schematic diagram of mechanical analysis of lifting pipe in deep-ocean mining

2 Nonlinear fatigue damage analysis methodology of deep-ocean lifting pipe

2.1 Multi-field coupling and multiple nonlinear vibration model

This section is based on the force analysis of deep-sea hydraulic lifting pipe (as shown in Fig. 2) and establishes a multi-field coupled multiple nonlinear vibration model for deep-sea lifting pipe. The specific modeling process is as follows:

(1) Vibration control equation

Based on the small deformation hypothesis and the Kirchhoff hypothesis [42], the lifting pipe displacement can be expressed as follows:

$$\begin{cases} u_1(z, t) = v_x(z, t), u_2(z, t) = v_y(z, t) \\ u_3(z, x, t) = v_z(z, t) - x \frac{\partial v_x}{\partial z}(z, t) - y \frac{\partial v_y}{\partial z}(z, t) \end{cases} \quad (1)$$

where $u_1(z, t)$, $u_2(z, t)$ and $u_3(z, t)$ are the displacement field function corresponding to coordinate system x, y, z (m); $v_x(z, t)$, $v_y(z, t)$ and $v_z(z, t)$ are the IL, CF and longitudinal displacement of lifting pipe, respectively (m).

The Green’s strain of lifting pipe can be expressed as follows:

$$\begin{cases} \varepsilon_{xx} = \frac{\partial u_1}{\partial x}, \varepsilon_{yy} = \frac{\partial u_2}{\partial y}, \varepsilon_{zz} = \frac{\partial u_3}{\partial z} + \frac{1}{2} \left(\left(\frac{\partial u_1}{\partial z} \right)^2 + \left(\frac{\partial u_2}{\partial z} \right)^2 \right) \\ \varepsilon_{xz} = \frac{1}{2} \left(\frac{\partial u_1}{\partial z} + \frac{\partial u_3}{\partial x} \right), \varepsilon_{yz} = \frac{1}{2} \left(\frac{\partial u_2}{\partial z} + \frac{\partial u_3}{\partial y} \right), \varepsilon_{xy} = \frac{1}{2} \left(\frac{\partial u_1}{\partial y} + \frac{\partial u_2}{\partial x} \right) \end{cases} \quad (2)$$

Substitute Eq. (1) into Eq. (2) to obtain:

$$\begin{cases} \varepsilon_{zz} = \frac{\partial v_z}{\partial z} - x \frac{\partial^2 v_x}{\partial z^2} - y \frac{\partial^2 v_y}{\partial z^2} + \frac{1}{2} \left(\left(\frac{\partial v_x}{\partial z} \right)^2 + \left(\frac{\partial v_y}{\partial z} \right)^2 \right) \\ \varepsilon_{xx} = \varepsilon_{yy} = \varepsilon_{xz} = \varepsilon_{yz} = \varepsilon_{xy} = 0 \end{cases} \quad (3)$$

where ε_{xx} , ε_{yy} , ε_{zz} , ε_{xy} , ε_{xz} and ε_{yz} are the six directions strain of lifting pipe unit; and x and y are the distance

from a particle on the lifting pipe unit to the axis along the x - and y -directions (m).

Because of the second Kirchhoff stress, ignoring Poisson effect, Hooke’s law under uniaxial stress is as follows:

$$\sigma_{zz} = E\varepsilon_{zz} \quad (4)$$

The potential energy of the lifting pipe can be expressed as follows:

$$U_P = \frac{1}{2} \int_V \sigma \varepsilon dV = \frac{1}{2} E \int_V \varepsilon^2 dV \quad (5)$$

Substitute Eqs. (3) and (4) into Eq. (5) to obtain:

$$U_P = \frac{E}{2} \int_0^L \int_A \left[v_z^2 + x^2 v_x''^2 + y^2 v_y''^2 + \frac{1}{4} (v_x'^2 + v_y'^2)^2 - 2xv_x'v_x'' - 2yv_y'v_y'' + 2xyv_x''v_y'' + v_z'(v_x'^2 + v_y'^2) - xv_x''(v_x'^2 + v_y'^2) - yv_y''(v_x'^2 + v_y'^2) \right] dAdz \quad (6)$$

where E is the elastic modulus of the lifting pipe material (Pa); A is the cross-sectional area of the lifting pipe (m²); L is the length of the lifting pipe unit (m) and $v'_i, i = x, y, z$ and $v''_i, i = x, y, z$ are the first-order and second derivative of the lifting pipe displacements with respect to z , respectively.

Because the infinitesimal segment of the lifting pipe is a standard cylindrical structure, according to the cylinder integral property, it can get:

$$\begin{aligned} \int AxdA &= \int AydA = \int AxydA = 0, \quad \int Ax^2dA \\ &= \int Ay^2dA = I \end{aligned} \quad (7)$$

Substitute Eq. (7) into Eq. (6) to obtain:

$$\begin{aligned} U_P &= \frac{E}{2} \int_0^L \left[Av_z'^2 + \frac{1}{4} A(v_x'^2 + v_y'^2)^2 + Av_z'(v_x'^2 + v_y'^2) \right. \\ &\quad \left. + Iv_x''^2 + Iv_y''^2 \right] dz = \frac{1}{2} \int_0^L \left[EA(v_z' + \frac{1}{2}(v_x'^2 + v_y'^2))^2 \right. \\ &\quad \left. + EI(v_x''^2 + v_y''^2) \right] dz \end{aligned} \quad (8)$$

The total kinetic energy of the lifting pipe is the sum of the kinetic energy of the pipe, the kinetic energy of the internal fluid, which can be expressed as follows:

$$T_K = \int_0^L \left\{ \int_A \left[\frac{\rho_v}{2} (\dot{u}_1^2 + \dot{u}_2^2 + \dot{u}_3^2) \right] dA + \frac{1}{2} A_i \rho_i (v_x^2 + v_y^2 + v_z^2) \right\} dz \tag{9}$$

where A_i is the internal cross-sectional area of the lifting pipe (m^2); ρ_i is the internal fluid density (kg/m^3); $\dot{u}_i, i = 1, 2, 3$ are the first-order derivative of the lifting pipe displacements field function with respect to time for coordinate system x, y, z (m/s) and v_x, v_y and v_z represent the absolute velocities of the internal fluid in the x -, y - and z -directions (m/s), which can be expressed as follows:

$$v_x = \dot{v}_x + Uv'_x, v_y = \dot{v}_y + Uv'_y, v_z = \dot{v}_z + U(1 + v'_z) \tag{10}$$

Substitute Eqs. (1), (7) and (10) into Eq. (9) to obtain:

$$T_K = \frac{1}{2} \int_0^L \left[m_v (\dot{v}_x^2 + \dot{v}_y^2 + \dot{v}_z^2) + \rho_v I (\dot{v}_x'^2 + \dot{v}_y'^2) + m_i ((\dot{v}_x + Uv'_x)^2 + (\dot{v}_y + Uv'_y)^2 + (\dot{v}_z + U(1 + v'_z))^2) \right] dz \tag{11}$$

where m_v is the mass of lifting pipe unit length (kg); $\dot{v}_i, i = x, y, z$ are the first-order derivative of the lifting pipe displacement with respect to time for the x -, y - and z -directions (m/s); m_i is the mass of the multiphase flow velocity in the lifting pipe unit (kg) and U is the multiphase flow velocity in the lifting pipe unit (m/s).

According to the variational principle ($\delta U_P|_{t=t_1,2/x=0,L} = \delta U'_P|_{t=t_1,2/x=0,L} = \delta \dot{U}_P|_{t=t_1,2/x=0,L} = 0$) and integration by parts ($\int f'(z)g(z)dz = f(z)g(z) - \int f(z)g'(z)dz$), the integration forms of U_P, T_K and W over time can be expressed as follows:

$$\begin{aligned} \delta \int_{t_1}^{t_2} U_P dt &= \frac{1}{2} \delta \int_{t_1}^{t_2} \int_0^L \left[EA \left(v'_z + \frac{1}{2} (v_x'^2 + v_y'^2) \right)^2 + EI (v_x''^2 + v_y''^2) \right] dz dt \\ &= \int_{t_1}^{t_2} \int_0^L \left[EA \left(v'_z + \frac{1}{2} (v_x'^2 + v_y'^2) \right) (\delta v'_z + v'_x \delta v'_x + v'_y \delta v'_y) + EI (v_x'' \delta v_x'' + v_y'' \delta v_y'') \right] dz dt \\ &= EA \int_{t_1}^{t_2} \int_0^L \left[\left(v'_z + \frac{1}{2} (v_x'^2 + v_y'^2) \right) (d\delta v_z + v'_x d\delta v_x + v'_y d\delta v_y) \right] dt + EI \int_{t_1}^{t_2} \int_0^L \left[(v_x'' d\delta v_x + v_y'' d\delta v_y) \right] dt \\ &= EA \int_{t_1}^{t_2} \left\{ \left[\left(v'_z + \frac{1}{2} (v_x'^2 + v_y'^2) \right) \cdot \right] \Big|_0^L - \int_0^L \left[\left(v'_z + \frac{1}{2} (v_x'^2 + v_y'^2) \right) v'_x \right]' + \left[\left(v'_z + \frac{1}{2} (v_x'^2 + v_y'^2) \right) v'_y \right]' \right] dz \right\} dt \\ &\quad + EI \int_{t_1}^{t_2} \left\{ (v_x'' \delta v_x + v_y'' \delta v_y) \Big|_0^L - \int_0^L [(v_x'')' d\delta v_x + (v_y'')' d\delta v_y] \right\} dt \\ &= -EA \int_{t_1}^{t_2} \int_0^L \left[\left(v'_z + \frac{1}{2} (v_x'^2 + v_y'^2) \right)' \delta v_z + \left[\left(v'_z + \frac{1}{2} (v_x'^2 + v_y'^2) \right) v'_x \right]' + \left[\left(v'_z + \frac{1}{2} (v_x'^2 + v_y'^2) \right) v'_y \right]' \right] dz dt \\ &\quad + EI \int_{t_1}^{t_2} \left\{ (v_x'' \delta v_x + v_y'' \delta v_y) \Big|_0^L - [(v_x'')' d\delta v_x + (v_y'')' d\delta v_y] \Big|_0^L + \int_0^L [(v_x'')'' \delta v_x + (v_y'')'' \delta v_y] dz \right\} dt \\ &= -EA \int_{t_1}^{t_2} \int_0^L \left[\left(v'_z + \frac{1}{2} (v_x'^2 + v_y'^2) \right)' \delta v_z + \left[\left(v'_z + \frac{1}{2} (v_x'^2 + v_y'^2) \right) v'_x \right]' \delta v_x + \left[\left(v'_z + \frac{1}{2} (v_x'^2 + v_y'^2) \right) v'_y \right]' \delta v_y \right] dz dt \\ &\quad + EI \int_{t_1}^{t_2} \int_0^L [(v_x'')'' \delta v_x + (v_y'')'' \delta v_y] dz dt \end{aligned} \tag{12}$$

$$\begin{aligned}
 \delta \int_{t_1}^{t_2} T_K dt &= \int_{t_1}^{t_2} \int_0^L \left\{ m_i \left[\begin{aligned} & m_v (\dot{v}_x \delta v_x + \dot{v}_y \delta v_y + \dot{v}_z \delta v_z) + \rho_v I (\dot{v}'_x \delta v'_x + \dot{v}'_y \delta v'_y) + \\ & (\dot{v}_x + U v'_x) \delta (\dot{v}_x + U v'_x) + (\dot{v}_y + U v'_y) \delta (\dot{v}_y + U v'_y) \\ & + (\dot{v}_z + U(1 + v'_z)) \delta (\dot{v}_z + U(1 + v'_z)) \end{aligned} \right] \right\} dz dt \\
 &= \int_0^L \left[\int_{t_1}^{t_2} \left\{ m_v (\dot{v}_x d v_x + \dot{v}_y d v_y + \dot{v}_z d v_z) + \rho_v I (\dot{v}'_x d v'_x + \dot{v}'_y d v'_y) \right\} \right. \\
 &\quad \left. + \int_{t_1}^{t_2} \left[\int_0^L \left\{ m_i \left[U (\dot{v}_x + U v'_x) d v_x + U (\dot{v}_y + U v'_y) d v_y + U (\dot{v}_z + U(1 + v'_z)) d v_z \right] \right\} \right] dt \right. \\
 &= \int_0^L \left[\begin{aligned} & m_v \left((\dot{v}_x \delta v_x + \dot{v}_y \delta v_y + \dot{v}_z \delta v_z) \Big|_{t_1}^{t_2} - \int_{t_1}^{t_2} (\ddot{v}_x \delta v_x + \ddot{v}_y \delta v_y + \ddot{v}_z \delta v_z) dt \right) \\ & + \rho_v I \left((\dot{v}'_x \delta v'_x + \dot{v}'_y \delta v'_y) \Big|_{t_1}^{t_2} - \int_{t_1}^{t_2} (\ddot{v}'_x \delta v'_x + \ddot{v}'_y \delta v'_y) dt \right) \\ & + m_i \left[(\dot{v}_x + U v'_x) \delta v_x + (\dot{v}_y + U v'_y) \delta v_y + (\dot{v}_z + U(1 + v'_z)) \delta v_z \right] \Big|_{t_1}^{t_2} \\ & - m_i \left[(\ddot{v}_x + U \dot{v}'_x) \delta v_x + (\ddot{v}_y + U \dot{v}'_y) \delta v_y + (\ddot{v}_z + U(1 + \dot{v}'_z)) \delta v_z \right] \end{aligned} \right] dz \\
 &\quad \left. + \int_{t_1}^{t_2} \left[\left\{ m_i \left[U (\dot{v}_x + U v'_x) \delta v_x + U (\dot{v}_y + U v'_y) \delta v_y + U (\dot{v}_z + U(1 + v'_z)) \delta v_z \right] \Big|_0^L \right. \right. \\
 &\quad \left. \left. - m_i \left[U (\dot{v}'_x + U v''_x) \delta v_x + U (\dot{v}'_y + U v''_y) \delta v_y + U (\dot{v}'_z + U(1 + v''_z)) \delta v_z \right] \right\} \right] dt \\
 &= \int_{t_1}^{t_2} \int_0^L \left[\begin{aligned} & -m_v (\ddot{v}_x \delta v_x + \ddot{v}_y \delta v_y + \ddot{v}_z \delta v_z) + \rho_v I (\ddot{v}''_x \delta v_x + \ddot{v}''_y \delta v_y) \\ & - m_i \left[(\ddot{v}_x + U \dot{v}'_x) \delta v_x + (\ddot{v}_y + U \dot{v}'_y) \delta v_y + (\ddot{v}_z + U(1 + \dot{v}'_z)) \delta v_z \right] \\ & - m_i \left[U (\dot{v}'_x + U v''_x) \delta v_x + U (\dot{v}'_y + U v''_y) \delta v_y + U (\dot{v}'_z + U(1 + v''_z)) \delta v_z \right] \end{aligned} \right] dz dt
 \end{aligned} \tag{13}$$

The virtual work by external excitation mainly includes ocean force, impact force of internal multi-phase flow, inertial force and viscous damping of fluid. The specific expression is as follows:

$$\begin{aligned}
 \delta W &= \int_0^L \left[\left(\begin{aligned} & F_D(z, t) + f_x(z, t) \\ & + F_x(z, t) - c \dot{v}_x \end{aligned} \right) \delta v_x \right. \\
 &\quad \left. + \left(\begin{aligned} & F_L(z, t) + f_y(z, t) \\ & + F_y(z, t) - c \dot{v}_y \end{aligned} \right) \delta v_y + \left(\begin{aligned} & f_z(z, t) \\ & + w_g - c \dot{v}_z \end{aligned} \right) \delta v_z \right] dz + \delta W_f
 \end{aligned} \tag{14}$$

where $F_D(z, t)$ and $F_L(z, t)$ are the drag force in the IL direction and the lateral lift in the CF direction (N), respectively; $f_x(z, t)$, $f_y(z, t)$ and $f_z(z, t)$ are the high-speed fluid impact loads in the lifting pipe in the x -, y - and z -directions (N), $F_x(z, t)$ and $F_y(z, t)$ are the additional mass inertia force of the fluid (N), w_g is the

longitudinal force of the lifting pipe (N) and W_f is fluid viscous damping (N). Among them:

$$\begin{cases} f_x(x, t) = -\rho_i A_i U^2 \sin[\alpha_2(t) - \alpha_1(t)] \cos[\varphi_2(t) - \varphi_1(t)] \\ f_y(x, t) = -\rho_i A_i U^2 \sin[\alpha_2(t) - \alpha_1(t)] \sin[\varphi_2(t) - \varphi_1(t)] \\ f_z(x, t) = -\rho_i A_i U^2 \cos[\alpha_2(t) - \alpha_1(t)] \\ c = 2m_v \omega_g \zeta, \omega_g = \pi^2 \sqrt{EI/m_v L^4} \\ w_g = m_v g - \rho_w \pi \frac{D^2}{4}, F_x(z, t) = m_a \ddot{v}_x, F_y(z, t) = m_a \ddot{v}_y \\ W_f = -\frac{1}{2} \pi D l \int_0^L \rho_i (1 + 2v'_z + v'^2_z) U^2 dz \end{cases} \tag{15}$$

where $\alpha_1(t)$, $\alpha_2(t)$, $\varphi_1(t)$ and $\varphi_2(t)$ are the deflection angles of the upper and lower micro-segments of the lifting pipe in the x - and y -directions (rad); ζ is the damping ratio; ρ_w is the density of seawater (kg/m^3);

D_o is the outer diameter of the lifting pipe (m); D_i is the inner diameter of the lifting pipe (m); f is the friction coefficient caused by fluid viscosity; m_a is the additional mass per unit length of pipe string (kg/m) and c is the damping coefficient.

According to Hamiltonian principle $\delta \int_{t_1}^{t_2} (U_P - T_K + W)dt = 0$, the vibration control equations of hydraulic lifting pipe in x -, y - and z -directions can be obtained as follows:

$$\left\{ \begin{aligned} &(m_v + m_a + m_i)\ddot{v}_x - \rho_v I \ddot{v}_x + c\dot{v}_x + 2m_i U \dot{v}_x' \\ &\quad + m_i U^2 v_x'' + EI v_x''' - EA \left((v_z' + \frac{1}{2}(v_x^2 + v_y^2)) v_x' \right)' \\ &= F_D(z, t) + f_x(z, t) \\ &(m_v + m_a + m_i)\ddot{v}_y - \rho_v I \ddot{v}_y + c\dot{v}_y + 2m_i U \dot{v}_y' \\ &\quad + m_i U^2 v_y'' + EI v_y''' - EA \left((v_z' + \frac{1}{2}(v_x^2 + v_y^2)) v_y' \right)' \\ &= F_L(z, t) + f_y(z, t) \\ &m_v \ddot{v}_z + c\dot{v}_z - EA (v_z'' + \frac{1}{2}(v_x^2 + v_y^2)') + \frac{1}{2} \pi D_i f \rho_i U^2 v_z'' \\ &= w_g + f_z(z, t) \end{aligned} \right. \tag{16}$$

The upper end of the lifting pipe is connected with a spherical joint, and the lower end is suspended with an intermediate chamber. The boundary conditions can be expressed as follows:

$$\left\{ \begin{aligned} &v_z(0, t) = u_{boat}(t), \quad \left[EA(v_z' + \frac{1}{2}(v_x^2 + v_y^2)) - m_i(U\dot{v}_z + U^2 v_z') + M_C \ddot{v}_z \right] \Big|_{(L, t)} = 0 \\ &v_x(0, t) = 0, \quad \left[\begin{aligned} &EA(v_x' + \frac{1}{2}(v_x^2 + v_y^2)) - (EI v_x'')' \\ &+ \rho_v I \ddot{v}_x - m_i(U\dot{v}_x + U^2 v_x') + M_C \ddot{v}_x \end{aligned} \right] \Big|_{(L, t)} = 0 \\ &v_y(0, t) = 0, \quad \left[\begin{aligned} &EA(v_y' + \frac{1}{2}(v_x^2 + v_y^2)) - (EI v_y'')' \\ &+ \rho_v I \ddot{v}_y - m_i(U\dot{v}_y + U^2 v_y') + M_C \ddot{v}_y \end{aligned} \right] \Big|_{(L, t)} = 0 \\ &EI v_x''|_{(0, t)} = 0, \quad EI v_x''|_{(L, t)} = 0, \quad EI v_y''|_{(0, t)} = 0, \quad EI v_y''|_{(L, t)} = 0 \end{aligned} \right. \tag{17}$$

where $u_{boat}(t)$ is the platform heave displacement (m), and M_C is the mass of the buffer station (kg).

(2) Analysis of outflow field

According to the Morison's equation, the drag force in the IL direction and the lateral lift in the CF direction can be expressed as follows:

$$\left\{ \begin{aligned} &F_D(z, t) = \frac{1}{2} \rho_w U_c^2 D_o \bar{C}_d - \rho_w U_c D_o \bar{C}_d \frac{\partial v_x}{\partial t} + \frac{1}{2} \rho_w U_c^2 D_o C_d' \frac{q_x}{2} \\ &F_L(z, t) = -\frac{1}{2} \rho_w U_c D_o \bar{C}_d \frac{\partial v_y}{\partial t} + \frac{1}{2} \rho_w U_c^2 D_o C_l' \frac{q_y}{2} \end{aligned} \right. \tag{18}$$

where U_c is the external flow velocity of lifting pipe (m/s); \bar{C}_d and \bar{C}_l are the steady-state drag force coefficient and lift force coefficient; C_d' and C_l' are the reference drag force coefficient and reference lift force coefficient and q_x and q_y are the dimensionless wake oscillator variables in the in-line flow direction and the cross-flow direction.

The fluid-structure interaction between the external flow field and the stress field of the riser structure can be described by the wake oscillator model [8]. According to Facchinetti and Langer's discussion on the coupling terms (displacement, velocity and acceleration) of wake oscillator, the calculated results of acceleration coupling are more consistent with the experimental results. The coupling between the structural vibration and the wake vibrator model is that the structural vibration affects the lift, which, in turn, affects the vibration of the structure. The control equation of the wake vibrator is as follows:

$$\left\{ \begin{aligned} &\ddot{q}_x + \varepsilon_x \omega_s (q_x^2 - 1) \dot{q}_x + (2\omega_s)^2 q_x = \frac{A_x}{D_o} \ddot{v}_x \\ &\ddot{q}_y + \varepsilon_y \omega_s (q_y^2 - 1) \dot{q}_y + (\omega_s)^2 q_y = \frac{A_y}{D_o} \ddot{v}_y \end{aligned} \right. \tag{19}$$

where ω_s is the shedding frequency of wake vortex, $\omega_s = 2\pi S_t |U_c - \dot{v}_x| / D_o$, S_t is the Strouhal coefficient and $\varepsilon_x, \varepsilon_y, A_x$ and A_y are dimensionless parameters determined by experiment, which are $\varepsilon_x = 1.2$, $\varepsilon_y = 0.3$, $A_x = 48$ and $A_y = 12$.

(3) Analysis of internal flow field

The ultimate settling velocity of spherical particles in still water is v_s , which is mainly determined by the balance of gravity, buoyancy and water drag. Ignoring secondary forces, the basic equation for settling velocity can be expressed as follows:

$$\frac{\pi d_p^3}{6} (\rho_s - \rho_i) g = \frac{\pi d_p^2}{8} C_p \rho_i v_s^2 \tag{20}$$

where d_p is the particle diameter (m); ρ_s is the density of solid particles (kg/m³) and C_p is the particle drag force coefficient.

The minimum water flow lifting speed is 3 times the maximum particle settling speed, and the minimum conveying speed for vertical lifting is as follows:

$$U = 3v_s = \sqrt{\frac{12(\rho_s - \rho_i)gd_p}{\rho_i C_p}} \tag{21}$$

A control equation for mixed two-phase flow in a riser is established without considering mass and heat exchange between phases, which can be expressed as follows:

$$\int_{\Delta V} \frac{\partial \rho_i}{\partial t} dV + \int_{\Delta V} \frac{\partial \rho_i U}{\partial z} dV = 0 \tag{22}$$

$$\begin{aligned} \frac{\partial}{\partial t} \int_{\Delta V} \rho_i U dV + \int_{\Delta V} \frac{\partial \rho_i U |U|}{\partial z} dV \\ = - \int_{\Delta V} \frac{\partial P}{\partial z} dV - \int_{\Delta V} \rho_i g \frac{\partial h \cos \alpha}{\partial z} dV - \int_A \tau_i dA \\ - \int_A \tau_m dA - \int_{\Delta V} \rho_i g \sin \alpha dV \end{aligned} \tag{23}$$

where ΔV is the selected control volume (m^3); P is the internal pressure (Pa); α is the inclination angle of pipe string ($^\circ$); h is the distance (m); τ_i is fluid viscous shear stress (Pa); τ_m is the wall shear stress (Pa) and λ_m is the wall friction coefficient.

(4) Heave motion equation of platform

It is necessary to establish the heave motion model of the platform under the action of random waves to determine the upper boundary displacement of the lifting pipe. According to Shen’s work [43], the heave motion equation of the platform can be expressed as follows:

$$m_p \ddot{u}_{boat}(t) + B_1 \dot{u}_{boat}(t) + B_2 u_{boat}(t) | \dot{u}_{boat}(t) | + \rho_w g A_w (u_{boat}(t) - \eta(t)) = \bar{F}_z \tag{24}$$

where m_p is the mass of the platform (kg), B_1 and B_2 are the heave radiation and heave viscous damping, respectively; A_w is the area of the platform at sea level (m^2) and $\eta(t)$ and \bar{F}_z are the surface displacements of the random wave (m) and random heave wave exciting force on the platform (N).

In this study, the Longuet–Higgins model [44] was used to simulate random wave surface displacement, which can be expressed as follows:

$$\eta(t) = \sum_{i=1}^M a_i \cos[\hat{\omega}_i t + \bar{\epsilon}_i] \tag{25}$$

where $\hat{\omega}_i (= (\omega_{i-1} - \omega_i)/2)$ is the circular frequency of the i -th harmonic (Hz), $\bar{\epsilon}_i$ is the initial phase of the i -th harmonic component (rad), taking the random number in the range $(0, 2\pi)$, M is the interval number

of the partition, $a_i (= \sqrt{2S(\omega)\Delta\omega})$ is the amplitude of the i -th harmonic component (m), $\Delta\omega (= (\omega_H - \omega_L)/N)$ is the frequency step and $S(\omega)$ is the random wave spectrum, which was described using the JONSWAP spectrum in this study. The expression for this obtained from Shen’s work [43] is as follows:

$$\begin{cases} S(\omega) = \frac{0.06238(1.094 - 0.01915 \ln \gamma)}{0.23 + 0.0336\gamma - 0.185(1.9 + \gamma)^{-1}} H_{1/3}^2 T_p^{-4} f^{-5} \\ \exp\left[-\frac{5}{4}(T_p f)^{-4}\right] \gamma^{\exp[-(f/f_p - 1)^2/2\sigma^2]} \\ T_p = \frac{T_{1/3}}{1 - 0.132(\gamma + 0.2)^{-0.559}}, \sigma = \begin{cases} 0.07, f \leq f_p \\ 0.09, f > f_p \end{cases} \end{cases} \tag{26}$$

where \bar{f} is the frequency (Hz), and ω is the circular frequency (Hz), $\omega = 2\pi f$; $H_{1/3}$ and $T_{1/3}$ are the significant wave height (m) and significant period (s) of the wave, f_p and T_p are the peak frequency (Hz) and peak period (s) of the wave, respectively; γ is the peak parameter, which is 3.3 in this study and σ is the peak shape coefficient.

In addition, according to Shen’s work, the random heave wave exciting force on the platform includes two parts: the exciting force of the random wave on the platform body ($F_s(t)$) and the exciting force of the random wave on the heave plate ($F_p(t)$), which can be expressed as follows:

$$\begin{aligned} \bar{F}_z &= F_s(t) + F_p(t) \\ &= 2\rho_w g \pi R^2 \left[1 - \frac{1}{2} \sin(kR) \right] \left(\frac{J_1(kR)}{kR} \right) e^{-kd} \eta(t) \\ &\quad + 0.597 \frac{\rho_w g}{4} \omega^2 e^{kz_{plate}} B_{plate}^3 \eta(t) \end{aligned} \tag{27}$$

where R is the platform radius (m), k is the wave number, $J_1(\cdot)$ is the first-order Bessel function of the first kind, d is the draft of the platform (m), z_{plate} is the depth of heave plate (m) and B_{plate} is the width of the heave plate (m).

(5) Solution scheme and experimental verification

In this study, the Newmark- β method and the Newton–Raphson method are used to jointly solve the vibration control equation of lifting pipe, and the fourth-order Runge–Kutta method is used to solve the wake oscillator model. The calculation code for the

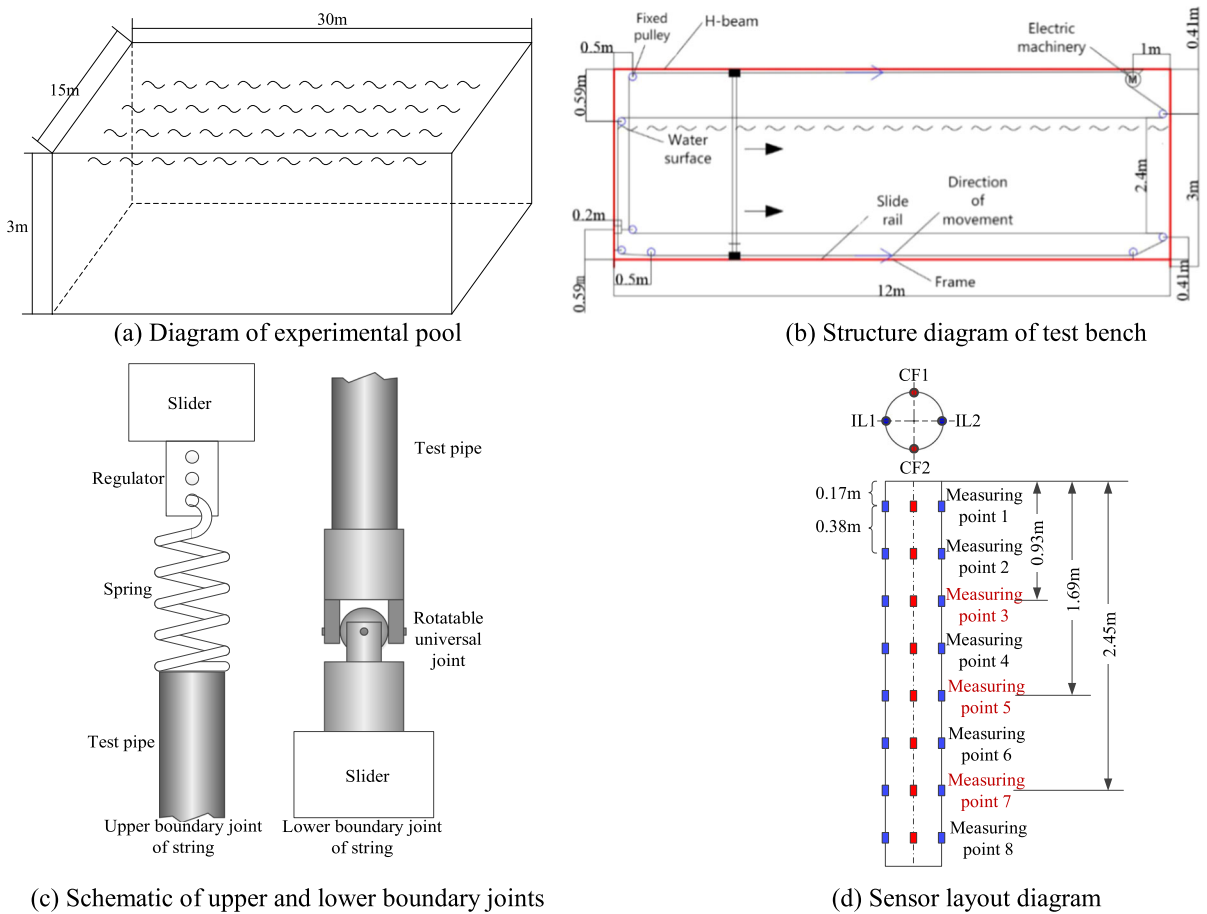


Fig. 3 Experimental system structures

nonlinear vibration model of the lifting pipe is written in Fortran language.

An experimental device for simulating vortex-induced vibration of lifting pipe is designed based on similarity principle, which is mainly composed of test pool, test bench, pipe string system, data testing system and gas supply and transmission system. In which, the size of the experimental pool is $30 \times 15 \times 3$ m (Fig. 3a). The test bench is mainly composed of test steel frame, winder, pulley, wire rope, rail, etc. (Fig. 3b). The experimental steel frame is welded by H-shaped steel, which is 12.5-m long and 3.5-m high. The fixed pulley is used to change the movement direction of the steel wire rope to ensure that the movement direction and speed of the top and bottom steel wire ropes are consistent. The use of steel wire rope to drag the movement of the experimental string can realize the synchronous movement of the

pipe, so as to ensure the force to simulate the uniform current. The upper end of the pipe is connected with the slider by a spring with elastic stiffness, and the lower end is connected with the lower slider by a rotary universal joint (Fig. 3c). The data testing system is composed of strain gauge, shielded wire and data acquisition instrument. The specific settings are shown in Fig. 3d. The gas supply and transmission system are composed of screw air compressor, high-pressure gas tank, connecting pipeline, flowmeter, solenoid valve, etc. Finally, the experimental system is built as shown in Fig. 4.

Figures 5 and 6, respectively, show the root-mean-square (RMS) distribution diagram of the displacement and the amplitude–frequency response curve of measuring point 3. Figure 5 shows that the displacement along the CF direction of the pipe column is significantly greater than the displacement along the



Fig. 4 Physical diagram of test system

IL direction. By comparing the test data with the model calculation results in this paper, it is found that the model calculation results are close to the test results, which verifies the correctness and effectiveness of the model in this paper.

Figure 6 shows that, regardless of the test results or the theoretical calculation results, the vibration frequency of the pipe in the IL direction is twice that in the CF direction, which is consistent with the results of the author's previous research [20, 21]. By observing the amplitude–frequency response results of measuring point 3, it is found that its vibration is obviously

complex, mainly due to the influence of external factors during the test process. At the same time, the calculation results in this paper are close to the test values, which again verifies the correctness of the established nonlinear vibration model.

2.2 Nonlinear fatigue damage model

In the service process of lifting pipe, fatigue damage accumulates continuously under the continuous action of load. The accumulation of fatigue damage will reduce the mechanical properties and bearing capacity

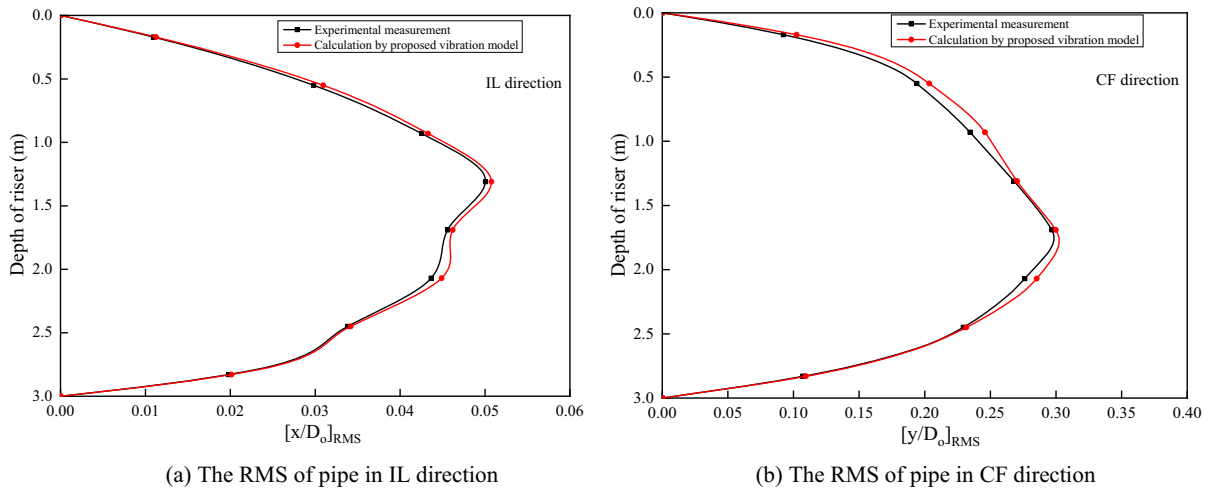


Fig. 5 The RMS distribution of pipe displacement

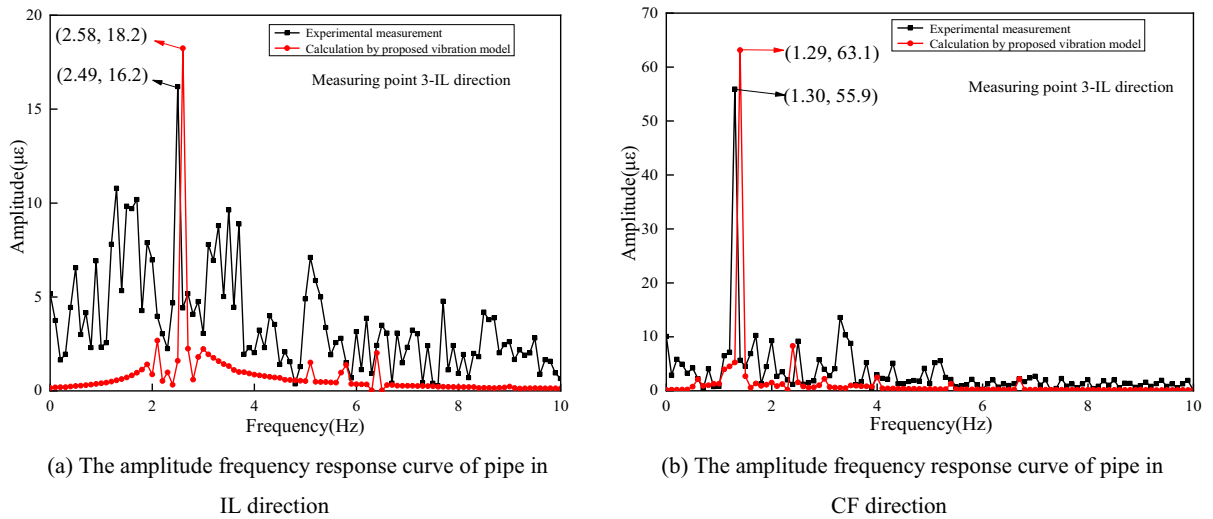


Fig. 6 The amplitude–frequency response curve of pipe at measuring point 3

of the lifting pipe, which, in turn, affects the accumulation of fatigue damage. The process of fatigue damage accumulation is also the process of residual strength degradation, and the two affect each other. Meanwhile, because the load on the lifting pipe is very complex, the interaction effect between the loads will also affect the fatigue damage of the lifting pipe. Therefore, this study will establish a nonlinear fatigue damage prediction method of deep-ocean lifting pipe based on load interaction effect and residual strength attenuation degradation.

Corten–Dolan cumulative damage method follows the exponential relationship between damage and cycle times, which can be expressed as follows:

$$D = prn^a \tag{28}$$

where D is fatigue cumulative damage after n constant amplitude stress cycles; p is the number of damage nuclei under stress; r is the damage coefficient and a is a constant related to the material.

According to Eq. (28), the critical fatigue damage D_c is

$$D_c = p_{\max} r_{\max} N_{\max}^a \tag{29}$$

where p_{\max} , r_{\max} and a_{\max} are, respectively, the number of damage nuclei, the damage coefficient and the material constant under the action of maximum stress. N_{\max} is the number of cycles under the action of maximum stress, i.e., fatigue life.

Under variable amplitude load, the fatigue cumulative damage can be established according to the total damage, that is, the sum damage of each section should be equal to that under constant amplitude load. Under the action of multistage variable amplitude load, the cumulative damage D_d is consistent with the critical fatigue damage D_c , that is:

$$D_d = \sum_{i=1}^k p_i r_i n_i^{a_i} = p_{\max} r_{\max} N_{\max}^{a_{\max}} \tag{30}$$

where i is the number of stress cycles. p_i , r_i , a_i and n_i are, respectively, the number of damage nuclei, the damage coefficient, the material constant and number of cycles under the action of i th stress.

For fatigue failure analysis, the fatigue life prediction formula of Corten–Dolan model under the multistage stress cycle can be expressed as follows:

$$N_f = \frac{N_{\max}}{\sum_{i=1}^k a_i \left(\frac{\sigma_i}{\sigma_{\max}}\right)^d} \tag{31}$$

where N_f is the fatigue life under multistage stress cycle, a_i is the percentage for the number of σ_i in the total number of cycles, σ_i is the i stress and σ_{\max} is the maximum stress in multistage stress. d is a parameter-related to material properties, loading sequence and residual strength. In this study, the d parameter is modified to take into account the load interaction and residual strength degradation effect of the lifting pipe.

Firstly, considering the interaction between lifting pipe loads and the contribution of small loads, the parameter d is modified. According to the work [45], this relationship can be reflected by introducing the ratio of stress at all levels to maximum stress, which can be expressed as follows:

$$d = \exp \left[\left(\frac{n_i}{N_{fi}} \right)^{\frac{\sigma_i}{\sigma_{\max}}} \right] + \lambda \tag{32}$$

where N_{fi} is the fatigue life under action of the single σ_i stress. λ is a constant related to the material, which can be determined by fitting according to the test data and fatigue failure criterion.

Many tests' data show that the cumulative fatigue damage is related to the loading order [46], for simple level two test loading, the cumulative fatigue damage at failure is often not equal to 1. When the loading sequence from low to high is adopted, the cumulative fatigue damage will be greater than 1 ($\sum (n_i/N_{fi}) > 1$). The crack initiation time should be delayed. When the loading sequence from high to low is adopted, the fatigue cumulative damage is less than 1 ($\sum (n_i/N_{fi}) < 1$). High stress makes the crack form in advance, and low stress makes the crack expand. According to the above analysis, when revising and defining the key parameter d , in addition to considering the influence of small load, real-time damage and stress state on fatigue cumulative damage, it is also necessary to further consider the influence of load loading sequence, so as to further improve the Corten–Dolan model. It can be expressed as follows:

$$d^* = \frac{\sigma_{i+1}}{\sigma_i} d = \frac{\sigma_{i+1}}{\sigma_i} \left\{ \exp \left[\left(\frac{n_i}{N_{fi}} \right)^{\frac{\sigma_i}{\sigma_{\max}}} \right] + \lambda \right\} \tag{33}$$

The residual strength degradation and the interaction between cyclic loads will have an impact on the subsequent cumulative damage, especially in the middle and late life of lifting pipe. With the continuous degradation for residual strength and mechanical properties of lifting pipe, the accumulation of fatigue damage will be accelerated. Considering the influence of residual strength degradation, the calculation of fatigue cumulative damage is more in-line with the actual damage process, which is of great significance to improve the accuracy of fatigue life prediction of lifting pipe. Different materials have different strength degradations regular pattern. At the initial stage of cyclic load, the defects caused by load have little effect on the lifting pipe. In the later stage of crack propagation, the reduction of effective stress area makes the strength of lifting pipe decrease rapidly and cause damage. Therefore, the residual strength degradation process of materials has the following characteristics:

- (1) The initial value of residual strength is equal to the tensile strength of the material, $R(0) = \sigma_b$;
- (2) At the time of fracture, the residual strength is equal to the peak fatigue load, $R(N) = \sigma_e$;
- (3) $R(n)$ is monotonically decreasing. At the initial time, the intensity degradation is very slow, and

it has the characteristics of “sudden death” when the cycle reach N .

The residual strength degradation model of materials under constant amplitude stress can be expressed as follows:

$$\frac{dR(n)}{dn} = -\sigma^{p'} R^{-q}(n) \tag{34}$$

where $R(n)$ is material residual strength, σ is cyclic stress and p' and q are the material constants, which can determine by material S–N curve. Integral on both sides of Eq. (34), it can be obtained:

$$\begin{aligned} R^{1+q}(n) &= R^{1+q}(0) - (1 + q)\sigma^{p'} n, \quad R(0) \\ &= \sigma_b, \quad R(N) = \sigma_e \end{aligned} \tag{35}$$

Equation (35) is the residual strength degradation model under constant amplitude load. In the case of multi-level load, it is assumed that there is k -level load, and the cycle is n_i under the stress σ_i . Then, the strength degradation expression for the i -th is as follows:

$$R_i^{1+q}(n_i) = R_{i-1}^{1+q}(n_{i-1}) - (1 + q)\sigma_i^{p'} n_i \tag{36}$$

By analogy, after experiencing the action of k -level load, the residual strength is as follows:

$$R_k^{1+q}(n_k) = R^{1+q}(0) - (1 + q) \sum_{i=1}^k \sigma_i^{p'} n_i \tag{37}$$

In order to characterize the rate of residual strength degradation, the residual strength degradation coefficient is defined as follows:

$$A_i = \frac{R_i(n_i)}{R_{i-1}(n_{i-1})} \tag{38}$$

where A_i is the strength degradation coefficient at i -th loading. Therefore, the residual strength can be expressed as follows after k -th loading:

$$R_{(k)}(n_k) = A_0 A_1 A_2 \cdots A_k R(0) \tag{39}$$

where A_0 is the strength degradation coefficient of initial moment when the load has not been loaded, and

the value of which is 1. We can define the strength degradation coefficient as follows:

$$A_{(k)} = A_0 A_1 A_2 \cdots A_k \tag{40}$$

Substituting Eqs. (37) ~ (39) into Eq. (40), it can be obtained:

$$A_{(k)} = \left[1 - \frac{(1+q) \sum_{i=1}^k \sigma_i^{p'} n_i}{R^{1+q}(0)} \right]^{\frac{1}{1+q}} \tag{41}$$

According to the logical relationship between cumulative damage and strength degradation coefficient, the strength degradation coefficient is introduced, and the exponential parameter d in Corten–Dolan model is defined as an exponential function related to strength degradation coefficient.

$$d^{**} = \exp\left(\lambda\left(\frac{1}{A_{(i)}} - 1\right)\right) \tag{42}$$

Since the load interaction and residual strength degradation effect are independent of each other, the two influencing factors can be taken into account in parameter d through direct superposition, and its expression is as follows:

$$\begin{aligned} d^{***} &= d^* + d^{**} \\ &= \frac{\sigma_{i+1}}{\sigma_i} \left\{ \exp\left[\left(\frac{n_i}{N_{fi}}\right)^{\frac{\sigma_i}{\sigma_{\max}}}\right] + \lambda \right\} \\ &\quad + \exp\left(\lambda\left(\frac{1}{A_{(i)}} - 1\right)\right) \end{aligned} \tag{43}$$

Substituting Eq. (43) into Eq. (31), the fatigue life prediction formula of Corten–Dolan model can be obtained:

$$N_f = \frac{N_{\max}}{\sum_{i=1}^k a_i \left(\frac{\sigma_i}{\sigma_{\max}}\right)^{\frac{\sigma_{i+1}}{\sigma_i}} \left\{ \exp\left[\left(\frac{n_i}{N_{fi}}\right)^{\frac{\sigma_i}{\sigma_{\max}}}\right] + \lambda \right\} + \exp\left(\lambda\left(\frac{1}{A_{(i)}} - 1\right)\right)} \tag{44}$$

2.3 Model validation

The correctness of the fatigue life prediction model established in this paper was verified using the experimental data of 7050-TT7451 aluminum alloy measured in Carvalho’s work [47]. The tensile

Table 1 Fatigue life of 7050-TT7451 aluminum alloy

Stress (MPa)	176	133	85
Fatigue life (cycle)	27,300	61,400	225,800

Table 2 Fatigue life prediction of 7050-TT7451 aluminum alloy under two-step load

Stress/ MPa	Number	$n_1/10^3$	$n_2/10^3$	Experimental life/ 10^3	Predicted life by Eq. (33)/ 10^3	Predicted life by Eq. (42)/ 10^3	Predicted life by Eq. (44)/ 10^3
176–133	1	2	47.4	49.4	59.02	37.09	47.23
	2	2	53.4	55.4	63.05	38.41	49.96
	3	4	60.1	64.1	65.07	36.99	62.53
	4	4	49.8	53.8	57.95	38.24	50.36
	5	13.6	14.2	27.8	34.2	31.56	30.56
	6	13.6	17.6	31.2	35.59	32.17	33.27
176–85	7	2	273.9	275.9	271.79	234.33	275.68
	8	2	271	273	268.53	199.12	269.34
	9	4	173.3	177.3	167.3	121.4	170.3
	10	4	231.7	235.7	214.52	185.17	221.93
	11	20.2	75.1	95.3	70.2	51.18	82.37
	12	10.8	69.8	80.6	81.84	51.86	76.83
133–85	13	5	191.8	196.8	198.27	105.42	195.62
	14	5	198.6	203.6	199.75	109.77	200.39
	15	10	229.4	239.4	210.27	99.16	224.65
	16	10	239.2	249.2	217.43	98.41	235.8

Table 3 The model calculation parameters

Parameters	Value	Parameters	Value
Length of pipe string (m)	2000	Seawater density (kg/m^3)	1025
Water depth (m)	2000	Pipe density (kg/m^3)	7850
Outer diameter of pipe (m)	0.44	Structural damping coefficient	0.01
Inner diameter of pipe (m)	0.40	Strouhal number	0.2
Elastic modulus of pipe (GPa)	207	Added mass coefficient	1.0
Number of elements	1000	Time step (s)	0.001

strength of 7050-TT7451 aluminum alloy measured in the test is 502 MPa, and the fatigue life under single-stage load is shown in Table 1.

According to the test data fitting, the S–N curve of 7070-T7451 aluminum alloy is $S^{2.903} \cdot N = 9.01 \times 10^{10}$, in which, it can be obtained that $p' = 2.903$, $q = 3.29$, $\lambda = 0.253$. First, the fatigue life of 7070-T7451 aluminum alloy only considering the influence of load loading sequence can be predicted using Eq. (33). Second, the fatigue life of 7070-T7451 aluminum alloy only considering the influence of residual strength degradation can be predicted using Eq. (42). Finally, the fatigue life of 7070-T7451 aluminum alloy both considering the influence of load loading sequence and residual strength degradation can be predicted using Eq. (44),

as shown in Table 2. By comparing with the experimental results, it is found that the fatigue prediction model established in this work has the highest calculation accuracy, which effectively verifies the correctness and effectiveness of the fatigue wear prediction model established in this manuscript.

3 Results and discussion

According to the working parameters (Table 3), the influences of outflow velocity, internal flow velocity and buffer station masses on fatigue characteristics of deep-ocean lifting pipe are investigated. The fatigue failure mechanism of lifting pipe is revealed, and a

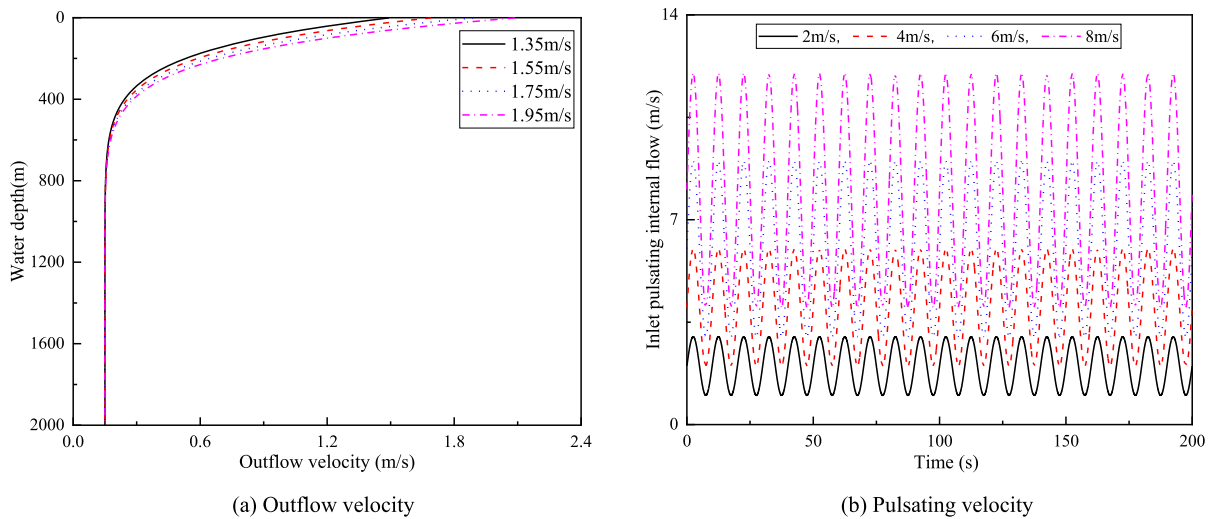


Fig. 7 The change curves of outflow velocity and pulsating velocity at the bottom of the lifting riser

safety control method was presented to improve service life of lifting pipe on-site.

In the Xiao's work [48], the external velocity can be expressed as follows: $U_c = 0.15 + U'_c \times \left(\frac{2000-z}{2000}\right)^{12}$, in which the U'_c is the sea-level velocity, and that is the variable in this study (Fig. 7a). The outflow velocity presents a nonlinear shear flow, which can be expressed as follows: $U = U_0 \left(1 + \mu \sin\left(\frac{2\pi}{T_0} t\right)\right)$, in that the parameters selected in this study are as follows: $\mu=0.5$, $T_0=10s$, and U_0 is internal velocity of seabed which is the variable in this study (Fig. 7b). Thus, the change curve of outflow velocity with water depth and the change curve of pulsating velocity at the bottom of the lifting riser can be calculated, as shown in Fig. 7.

3.1 Nonlinear vibration characteristics of lifting pipe

Figure 8 shows the time-space distribution cloud diagram of the vibration response for the deep-ocean mining lifting pipe under different towing speeds and pulsating velocities. It can be seen that the vibration is mainly controlled by the traveling wave. Due to the input of the internal flow at the bottom, the fluid at the lower part is all traveling wave response. With the increase in towing speed (as shown in Fig. 8d ~ p), the traveling wave and standing wave responses of the lifting pipe become more and more, and the energy input is also increased. The lifting pipe also changes

from the low-order mode to the high-order mode, and the vibration energy distribution of the riser along the water depth direction is more uniform. With low towing speed (Fig. 8a), the vibration displacement at the upper part of the pipe is larger, and with high towing speed (Fig. 8i), the vibration displacement at the middle part of the pipe is larger. Therefore, with the increase in the towing speed, the easily failed position of the pipe shifts from the upper to the middle part, and the designer needs to focus on it.

With the increase in lifting speed (as shown in Fig. 8a ~ d), the standing wave area gradually decreases, and the traveling wave area gradually increases. The velocity of internal flow will affect the energy input area. Under the action of high lifting speed and high towing speed (as shown in Fig. 8p), the propagation direction of traveling wave will produce multiple directions. It is worth noting that the region near the top of the lifting pipe is always controlled by the standing wave response, regardless of the internal and external flow changes. Meanwhile, with the increase in lifting speed, the vibration displacement at the upper part of the riser generally shows a trend of first decreasing and then increasing. The main reason is that with the increase in lifting speed, although the internal excitation is increased, the vibration of the lifting pipe will increase, but the mass of the internal flow field unit will also increase correspondingly, which effectively reduces the vibration of the lifting pipe. In the early stage, the effect of suppressing the

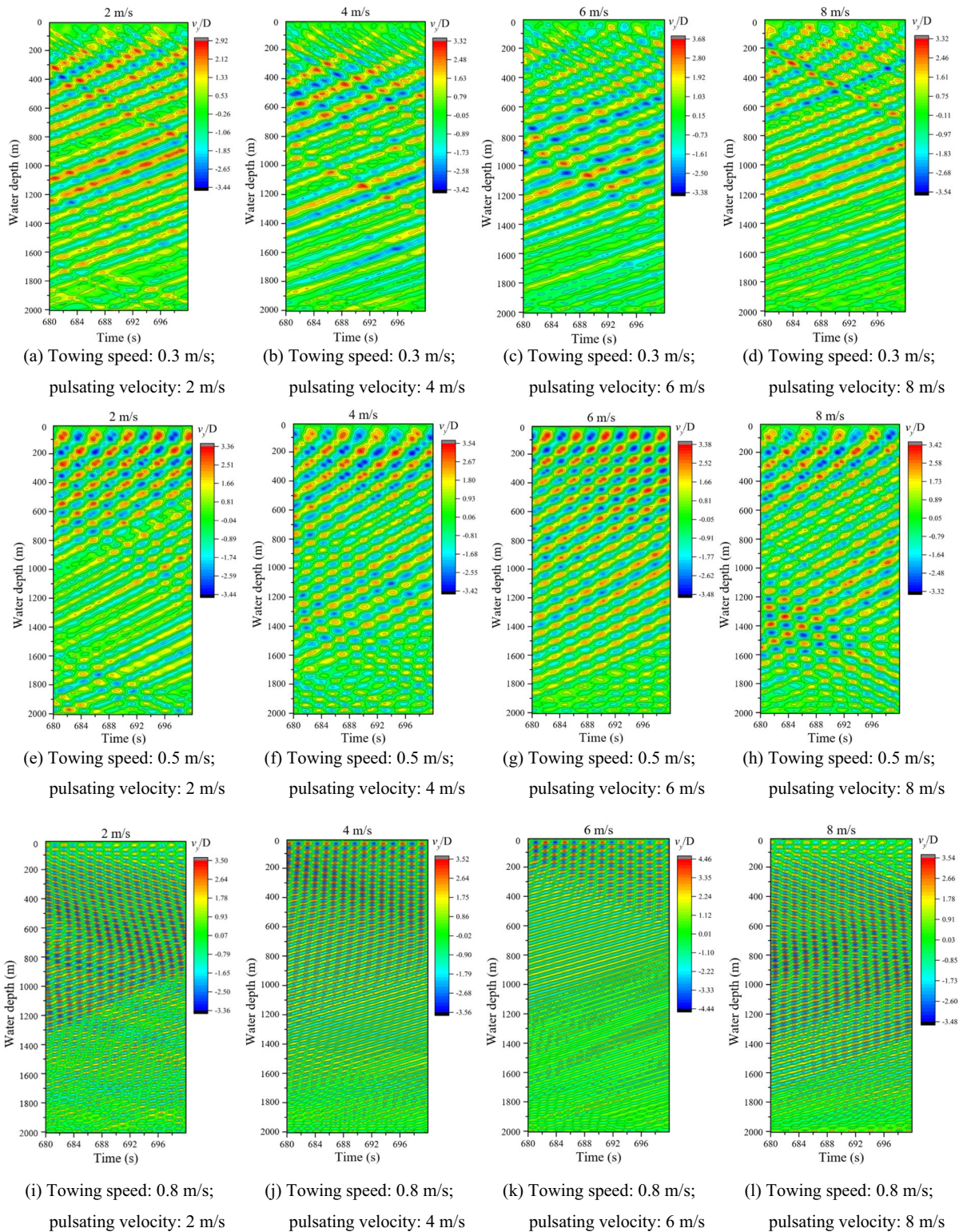


Fig. 8 Standing wave and traveling wave responses of the lifting riser under different towing v speeds and pulsating velocities

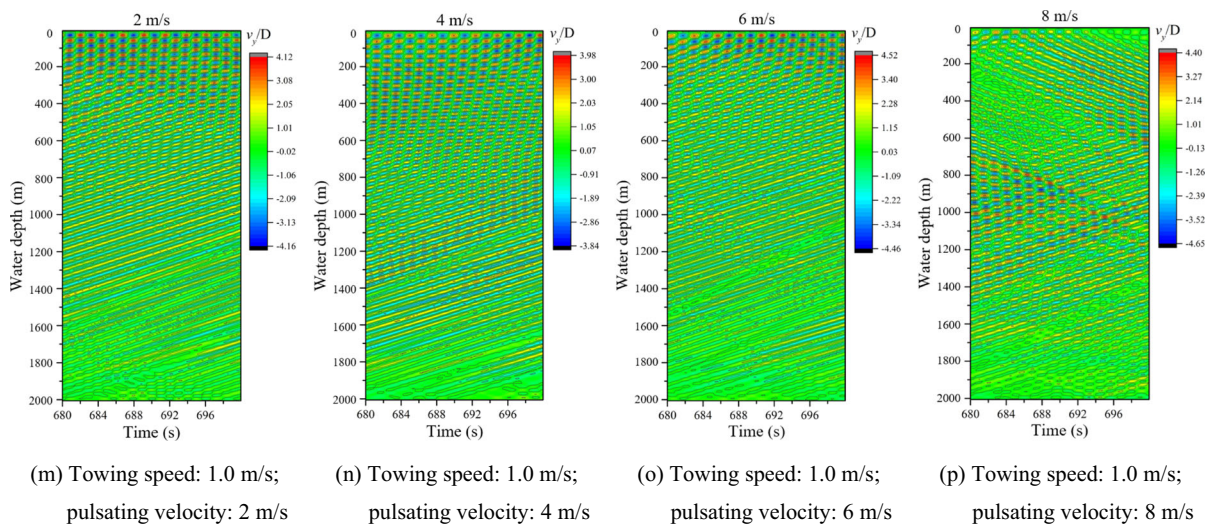


Fig. 8 continued

vibration of the lifting pipe is greater, which leads to the decrease in the displacement. When the lifting speed reaches a certain level, the effect of increasing the internal excitation is greater, which leads to the increase in the displacement.

Figure 9 shows phase diagram and Poincare map of the lifting pipe at a water depth of 1200 m under different towing speeds and lifting speeds. As shown in Fig. 9a~d, when the towing speed is 0.3 m/s, the influence of different lifting speeds on the phase trajectory morphology of the vibration of the lifting pipe is not obvious, and strange attractors and fractal Poincare maps are formed in the phase space. It indicates that the riser presents complex and irregular vibration in this state. However, with the increase in the lifting speed, the vibration of the riser shows a trend of decreasing first and then rising. When the lifting speed is 8 m/s, the vibration is the most complex. Figure 9e~h shows that, when the towing speed is 0.5 m/s, the vibration amplitude becomes larger, and the discrete points of Poincare map become more and more. The vibration of the lifting pipe is also chaotic. With the increase in the lifting speed, the Coriolis force and centrifugal force caused by the internal flow increase, resulting in the more obvious influence of the internal flow on the pipe, thus making the internal structure of the attractor formed in the phase space more abundant. With the increase in the towing speed, the vibration state of the lifting pipe transits from the chaotic motion of the phase trajectory

to the toroidal motion of the phase trajectory. However, the discrete points of the Poincare map still have fractal characteristics, and the vibration of the lifting hard pipe is still in a chaotic state.

Figure 9i~l shows that, when the lifting speed increases from 2.0 to 6.0 m/s under the towing speed is 0.8 m/s, the torus of its phase trajectory gradually converges and tends to converge to the limit cycle. However, when the velocity increases from 6.0 to 8.0 m/s, the torus of its phase trajectory expands again. It can be seen from Fig. 9m~p that, when the towing speed is 1.0 m/s, the phase trajectories of the lifting pipe are all toroidal. With the increase in the lifting speed, the toroidal distribution is more uniform. As the vibration of vertically and horizontally coupled nonlinear lifting hard pipe is highly nonlinear, when the external flow and the internal lifting flow velocity are high, its phase trajectory presents a torus, but the vibration is always chaotic, and it is difficult to form periodic or quasi-periodic motion.

3.2 Influence of the outflow velocity

Ocean load is one of the most important external loads of hydraulic lifting riser. The main factor determining the size of ocean load is the external velocity, and this paper considers the nonlinear distribution effect of external velocity with water depth. Under the action of different outflow velocities, the lifting riser presents different vibration states, which affects the fatigue life

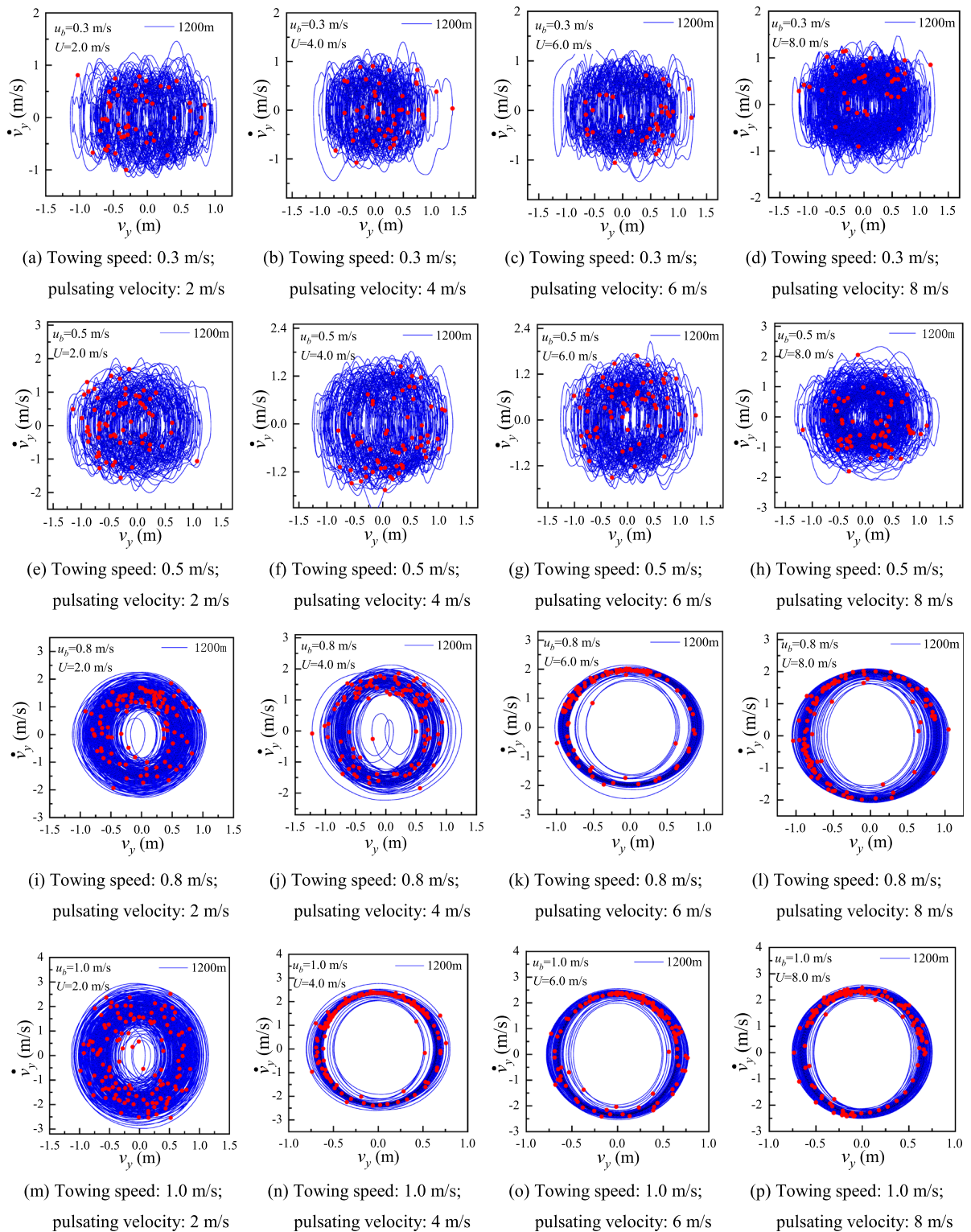


Fig. 9 Phase trajectories and Poincaré map of the lifting riser under different towing speeds and pulsating velocities

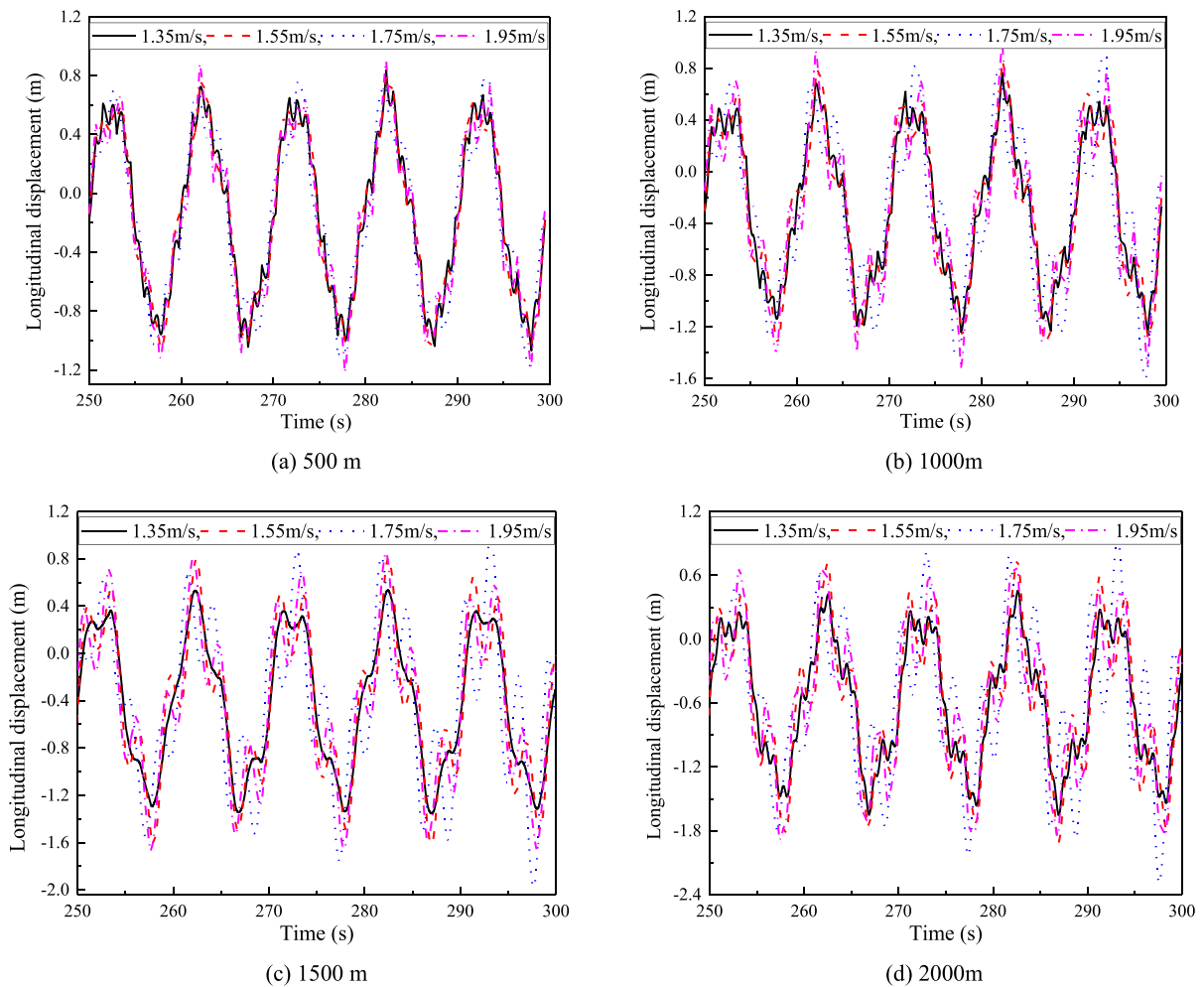


Fig. 10 Longitudinal displacement of lifting pipe at different positions under different outflow velocities

of the lifting pipe. Therefore, in this study, the outflow velocity is set as 1.35, 1.55, 1.75 and 1.95 m/s, and keeping the internal flow velocity and buffer station masses unchanged, which are, respectively, set as 2 m/s and 150 t. The other calculation parameters listed in Table 3. The curves of displacement in three direction, maximum axial stress, dominant frequency and fatigue life corresponding to different positions of lifting pipe are obtained, as shown in Figs. 10, 11, 12 and 13. In order to display the fatigue life of lifting pipe conveniently, once the fatigue life is more than 60 years, it is considered as 60 years.

Figure 10 shows the longitudinal displacement of the hydraulic lifting riser at different positions under different outflow velocities. It can be seen that the longitudinal vibration of the riser presents periodic

vibration as a whole, and high-frequency nonlinear vibration occurs locally.

The periodic vibration is mainly caused by its self-gravity, while the local high-frequency nonlinear vibration is mainly caused by lateral nonlinear vibration. Because the nonlinear vibration model established in this paper considers the vertical and horizontal coupling effects. Meanwhile, it is found that the longitudinal vibration amplitude increases from top to bottom (Fig. 10a ~ d). The main reason is that the gravity effect is taken into account, and the deformation of the riser itself is superimposed from top to bottom. Moreover, the vibration displacement of the riser at each position changes up and down with a negative value as the center, indicating that the vibration balance position of the riser moves upward.

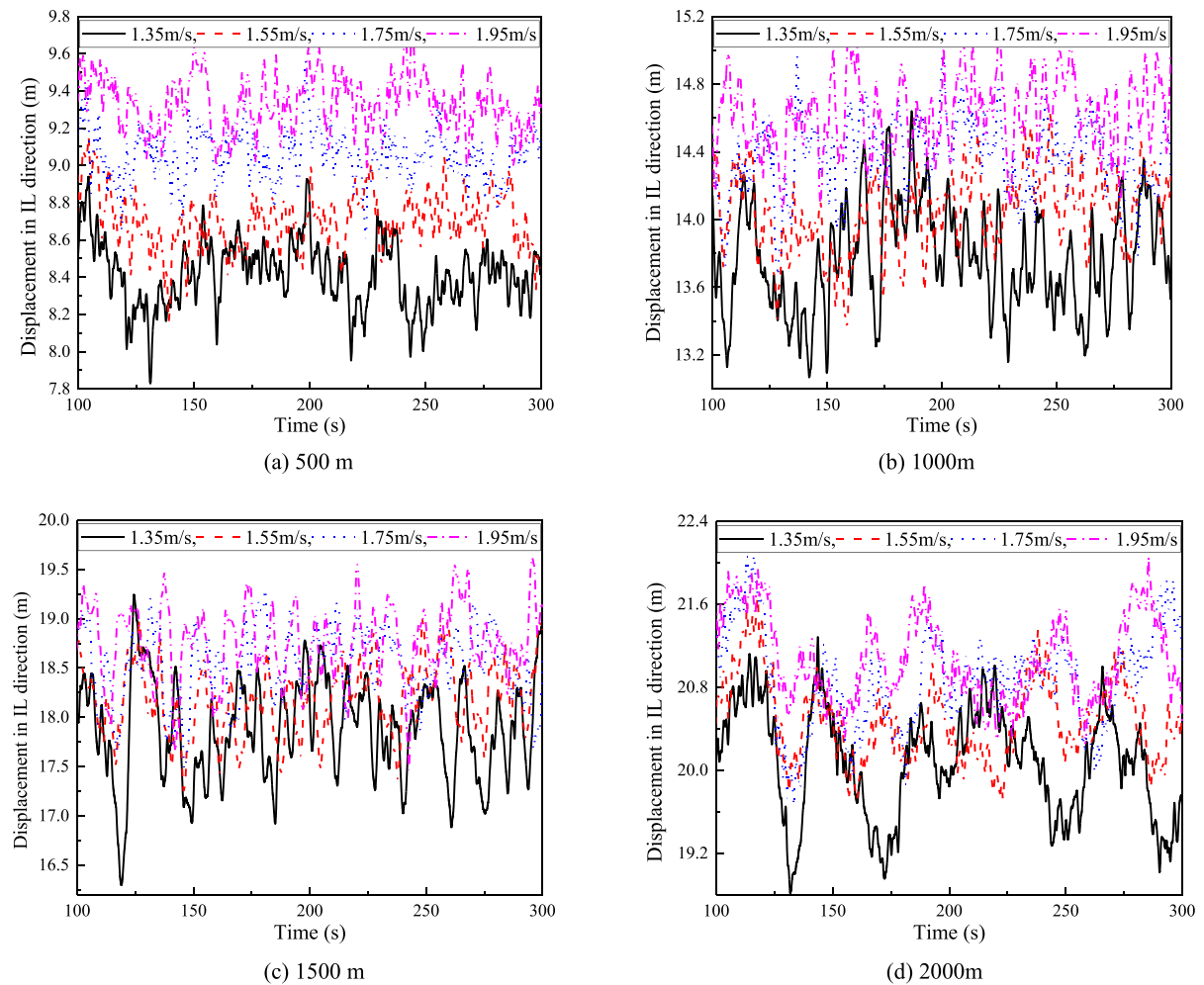


Fig. 11 Displacement in IL direction of lifting pipe at different positions under different outflow velocities

The main reason for this phenomenon is that the model in this paper considers the heave motion of the offshore platform, and the offshore platform floats upward under the action of waves, so that the overall balance position of the riser below also moves upward. With the increase in the outflow velocity, the longitudinal vibration displacement of the riser increases correspondingly, but the change is small. The main reason is that the change of the outflow velocity mainly affects the lateral vibration of the riser and then affects the longitudinal vibration of the riser. Therefore, when the riser is faced with high outflow velocity, it is necessary to focus on the lateral vibration of the riser.

Figure 11 shows the displacement along IL direction of the hydraulic lifting riser at different positions

under different outflow velocities. It can be noted that the vibration displacement along the IL direction of the riser increases from top to bottom. The main reason is that the lower boundary of the riser is a free end, which presents a similar suspension structure. Under the action of ocean load, it naturally presents a swaying state. As the ocean load changes along the water depth direction, it presents nonlinear characteristics, resulting in the riser offset rate also presents nonlinear characteristics. At the same time, it is found that the displacement along the IL direction of the riser is larger than that in the longitudinal and CF directions, but the vibration amplitude is smaller than that in the longitudinal and CF directions. The main reason is that the IL displacement of the riser includes two parts. One part is the drift caused by the steady-

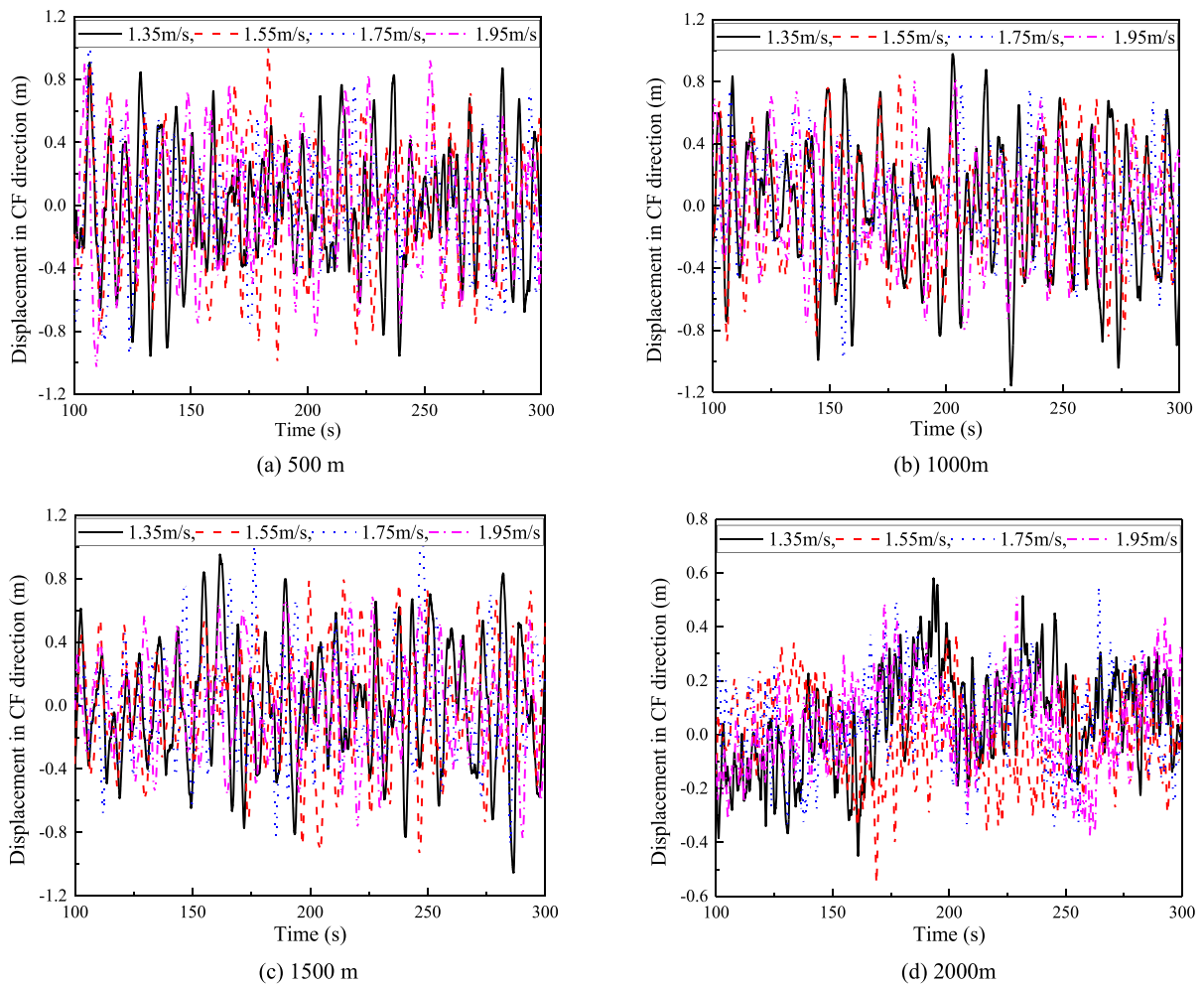


Fig. 12 Displacement in CF direction of lifting pipe at different positions under different outflow velocities

state drag force generated by the ocean current against the riser (this part of displacement can reach about 20 m at the bottom of the riser, as shown in Fig. 11d), and this part is the main load causing the plastic deformation of the riser. The other part is the vibration displacement caused by the pulsating drag force generated by the ocean current against the riser, which is the main load causing the fatigue failure of the riser. It is shown that the bending stress of the riser in the IL direction is large, and the plastic deformation of the riser in this direction should be focused on. However, the bending stress amplitude is not large, and the vibration in this direction has the smallest contribution to the fatigue damage of the riser (relative to the longitudinal vibration and the CF vibration). Moreover, with the increase in the outflow velocity, the

vibration displacement of the riser in the IL direction presents an increasing trend, and the vibration displacement change trend of the upper riser (the change value is about 1 m) is greater than that of the lower riser (the change value is about 0.8 m), as shown in Fig. 11a and d. The main reason is that the ocean velocity changes from large to small with the water depth (Fig. 7a). Therefore, with the increase in the ocean velocity, the upper end velocity changes obviously, resulting in a more significant increase in the drag force, and finally, the vibration displacement of the upper end riser changes significantly.

Figure 12 shows the displacement along CF direction of the hydraulic lifting pipe at different positions under different outflow velocities. It can be observed that the CF vibration displacement of the lifting pipe

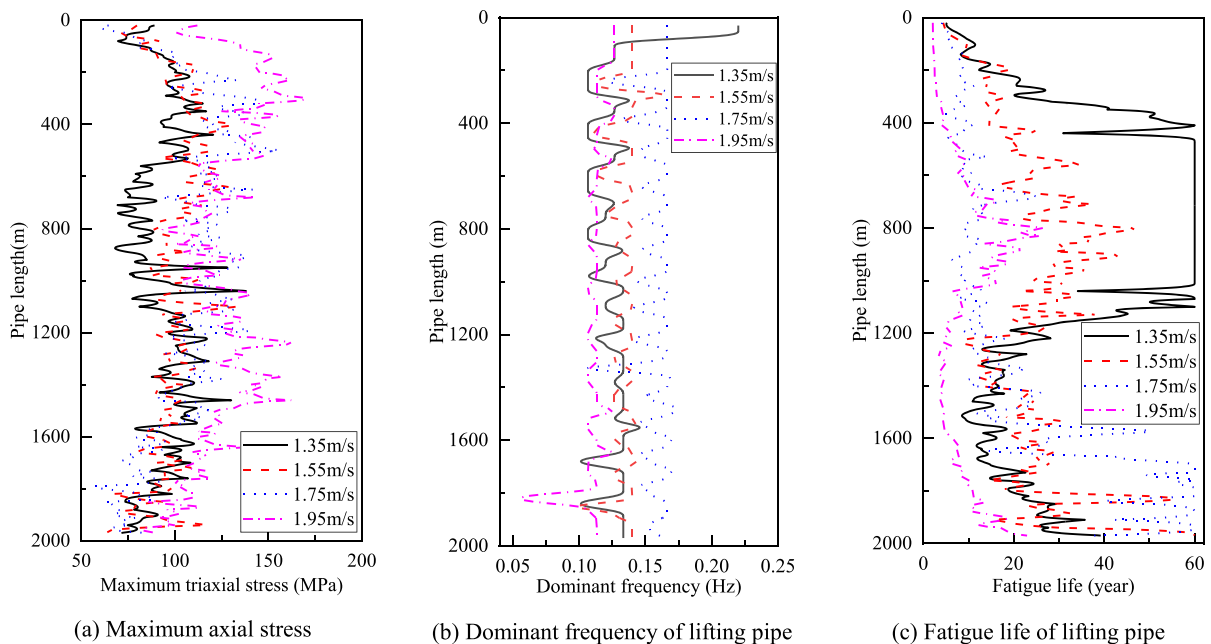


Fig. 13 Fatigue damage analysis data of lifting pipe under different outflow velocities

varies around 0, and the vibration amplitude is slightly larger than the IL vibration amplitude. The main reason is that for the cylindrical structure, the steady-state lifting force is 0, and only the pulsating lifting force generated by the ocean load. Therefore, there is no stable drift displacement. The upper displacement of the riser is greater than the bottom displacement due to the influence of the upper high-velocity zone (Fig. 12a and d). The vibration of the lifting pipe at low-flow rate and high-flow rate has nonlinear characteristics. When the vortex shedding frequency is related to the vibration speed of the lifting pipe, the vortex shedding frequency is no longer a fixed value, and the lift and drag force changes are not periodic, resulting in more complex dynamic phenomena of the lifting pipe. With the increase in the velocity at the upper end of the outflow, the vibration frequency in the middle part changes slightly (Fig. 12b and c), but the amplitude becomes larger, and the vibration at the bottom is more complex (Fig. 12d). This is because the flow velocity difference in the middle part is small, resulting in little change in its vibration frequency. However, the high-frequency vibration of the upper part will affect the vibration response of the middle part. The bottom part is the free end and is affected by the buffer station mass. It is sensitive to changes in external factors, and the vibration response is

complex. The frequency of vortex-induced vibration in the CF direction of the lifting pipe increases with the increase in the outflow velocity. When the speed is high, that is, the frequency band distribution of vortex-induced vibration in the CF direction of the deep-sea lifting pipe is wider. The higher flow speed can excite higher-order frequencies, and the lower-order frequencies will also be excited together. This is because the high-flow speed will cause the vortex shedding frequency to change in a larger range, resulting in a larger frequency change range of the excitation force (lift force). It makes the frequency of vortex-induced vibration in the CF direction of the lifting pipe more complex and also generates more frequency bands.

Figure 13 shows fatigue damage analysis data of lifting pipe under different outflow velocities including maximum axial stress, dominant frequency and fatigue life of the lifting pipe. It can be noted that the maximum stress of the pipe occurs at the position of 300 ~ 600 m in the middle and upper part (1/6 ~ 1/3 of the pipe) and at the position of 1200 ~ 1600 m in the middle and lower part (3/4 ~ 4/5 of the pipe). With the increase in the external flow velocity, the maximum triaxial stress of the riser shows an increasing trend (as shown in Fig. 13a). The main reason is that the lifting pipe is affected by ocean load. Its maximum stress also appears at the upper “one-

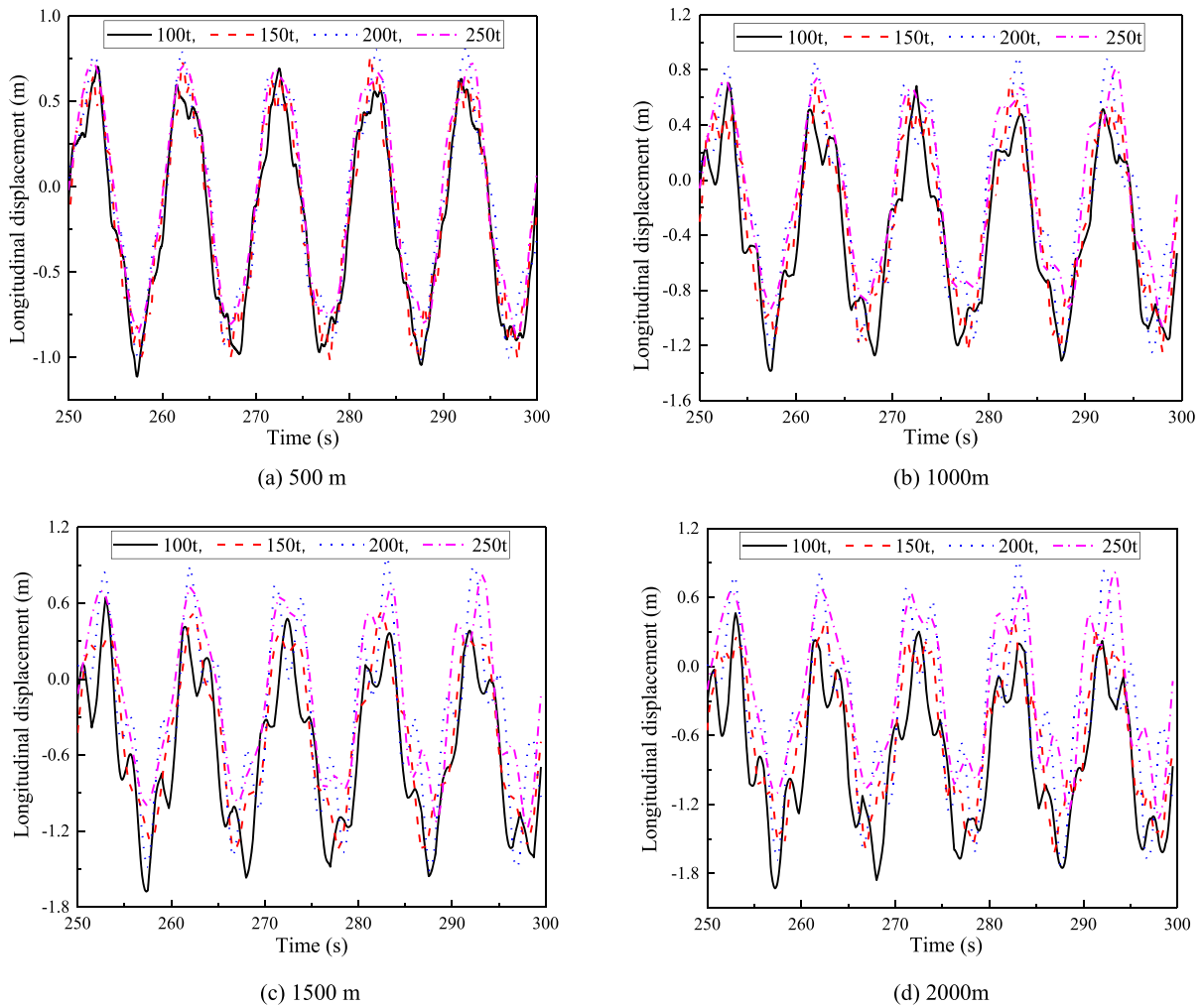


Fig. 14 Longitudinal displacement of lifting pipe at different positions under different buffer station masses

third” position, which was called “one-third effect” by academician Zhou et al. [49]. This is mainly because the ocean load presents a distribution state of large upper end and small lower end, which is similar to the shear distribution. Through the force analysis, its action point is just located at the upper one-third position. It can be seen from Fig. 13b, at different positions, the dominant frequency of the pipe does not change significantly. With the increase in the external flow rate, the main frequency of the pipe tends to decrease first and then increase. The main reason is that with the increase in the external flow rate, the vibration amplitude of the pipe increases, resulting in the reduction of the vibration frequency of the riser. Later, when the external excitation frequency is far

higher than the natural frequency of the pipe, the vibration amplitude of the pipe decreases, and the vibration frequency increases. Figure 13c shows the fatigue life of lifting pipe at different positions. It can be seen that the fatigue life of the upper end of the pipe and the middle and lower positions is the lowest. The main reason why the upper end of the riser is prone to fatigue damage is that the vibration frequency at the upper end is large, and the maximum triaxial stress at the position where fatigue damage is prone to occur at the middle and lower parts of the riser is the largest. Therefore, the site designer should pay attention to the fatigue damage at this position, and set some special fatigue resistant materials at this position, or reduce the vibration displacement and frequency at these

positions. With the increase in the outflow velocity, the fatigue life of the pipe tends to decrease first and then increase, and an external flow rate with the maximum fatigue life appears. However, in real operation, the external flow rate cannot be controlled. Therefore, according to a certain external flow rate, the optimal structure setting can be evaluated by changing the structure of the riser and the analysis method established in this paper to improve the service life of the lifting pipe.

3.3 Influence of buffer station masses

The buffer station is mainly installed at the tail of the lifting pipe. Since the lower part is connected with the lifting hose, it can be moved at will. The buffer station

is set as the free end in this paper, only its mass effect is considered, and the influence of its size is ignored. The different qualities directly affect the vibration response and fatigue life of the whole pipe system, and the corresponding optimization method is also the focus of field personnel. Therefore, it is necessary to reasonably design the mass of the buffer station. In order to explore the influence of the buffer station mass on the vibration response and fatigue life of lifting pipe, the buffer station masses are set as 100, 150, 200 and 250 t, respectively. And keeping outflow velocity and the internal flow velocity unchanged, which are, respectively, set as 1.35 and 2 m/s. The curves of displacement in three directions, maximum axial stress, dominant frequency and fatigue life

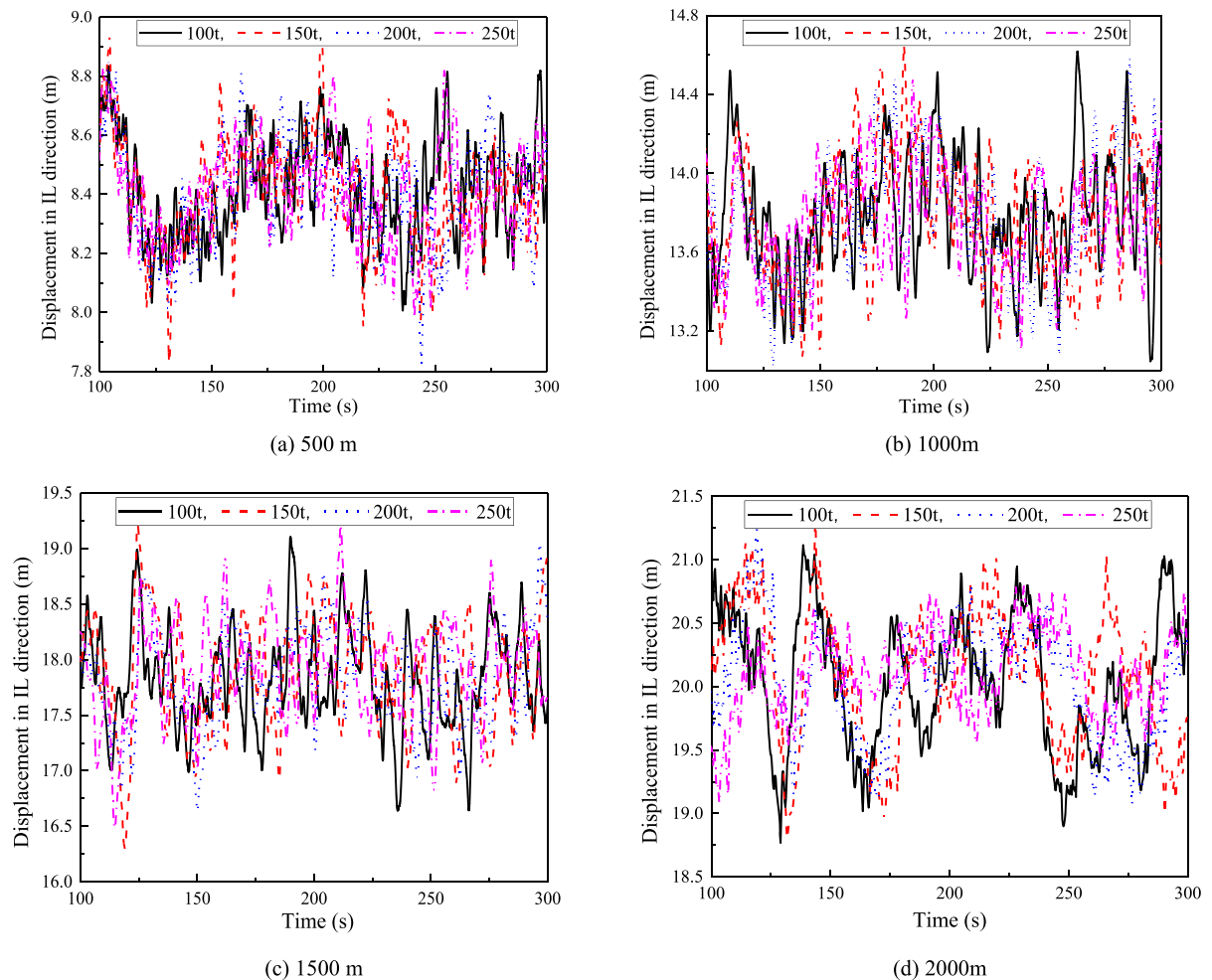


Fig. 15 Displacement in IL direction of lifting pipe at different positions under different buffer station masses

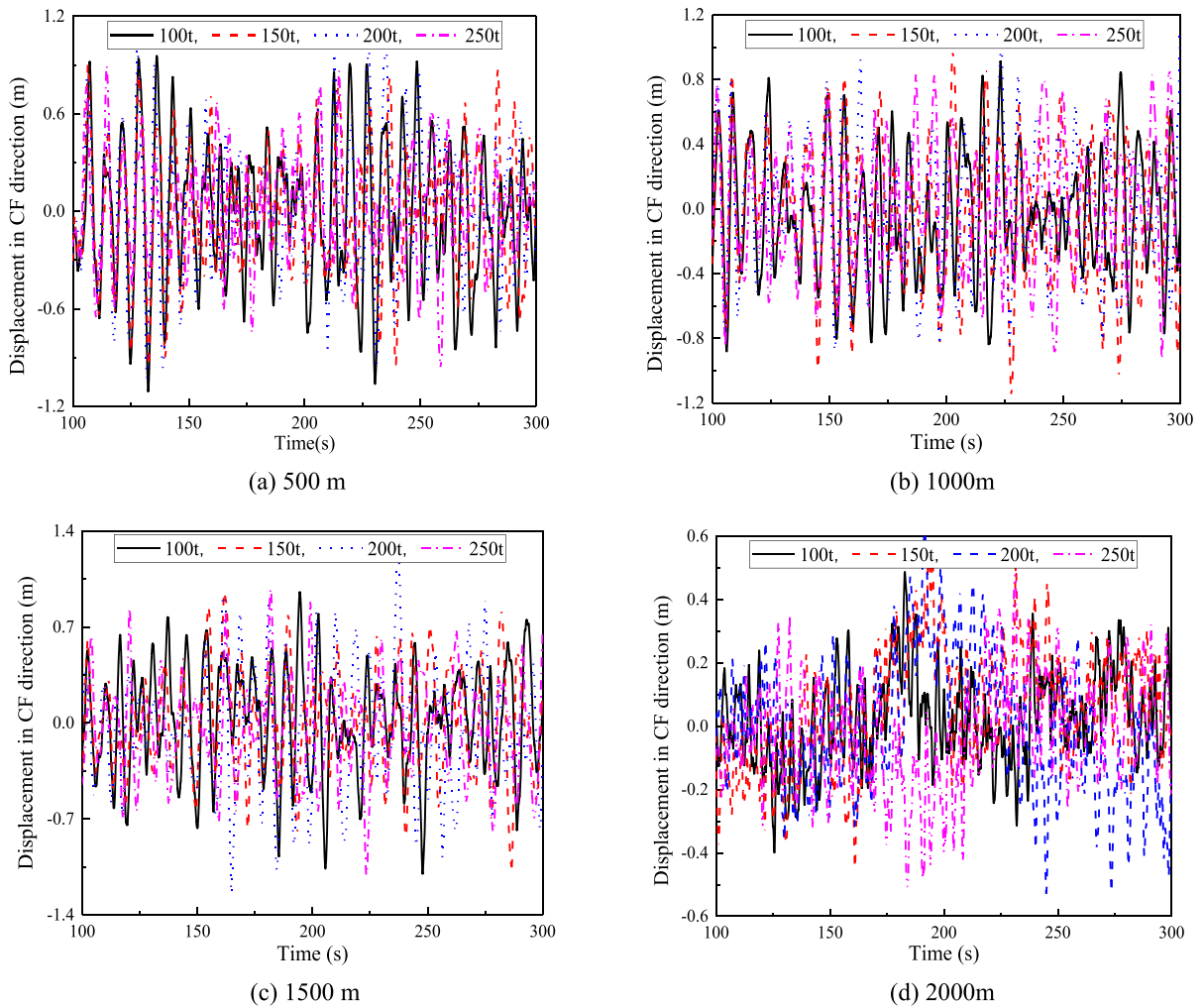


Fig. 16 Displacement in CF direction of lifting pipe at different positions under different buffer station masses

corresponding to different positions of lifting pipe, are obtained.

Figure 14 shows the longitudinal displacement of lifting pipe at different positions under different buffer station masses the larger the buffer station mass, it can be seen that, with the increase in the buffer station mass, the longitudinal displacement of all positions of the lifting pipe also increases. However, the displacement trend of the upper end of the pipe is much smaller than that of the lower end (Fig. 14a and d). When the buffer station mass is 200 t, the maximum vibration displacement occurs (Fig. 14c and d). The main reason is that the increase in buffer station mass not only increases the longitudinal force of the pipe, but also affects the natural frequency of itself. As a result,

when the buffer station mass is 200 t, the frequency of pipe is similar to that of the external excitation, and the secondary cumulative increase in the pipe vibration occurs. Moreover, the balance point at the lower end of the pipe changed from a negative value with buffer station mass is 200 t to a positive value with buffer station mass is 250 t (Fig. 14d). The main reason is that with the increase in the buffer station mass, the gravity of the lifting pipe increases, which makes the overall deformation move downward (the numerical value is positive), and the cumulative effect of the lower end position is the largest, making the balance position of the pipe at the lower end change from compression to tension. Therefore, when the buffer station mass is configured on-site, on the premise of

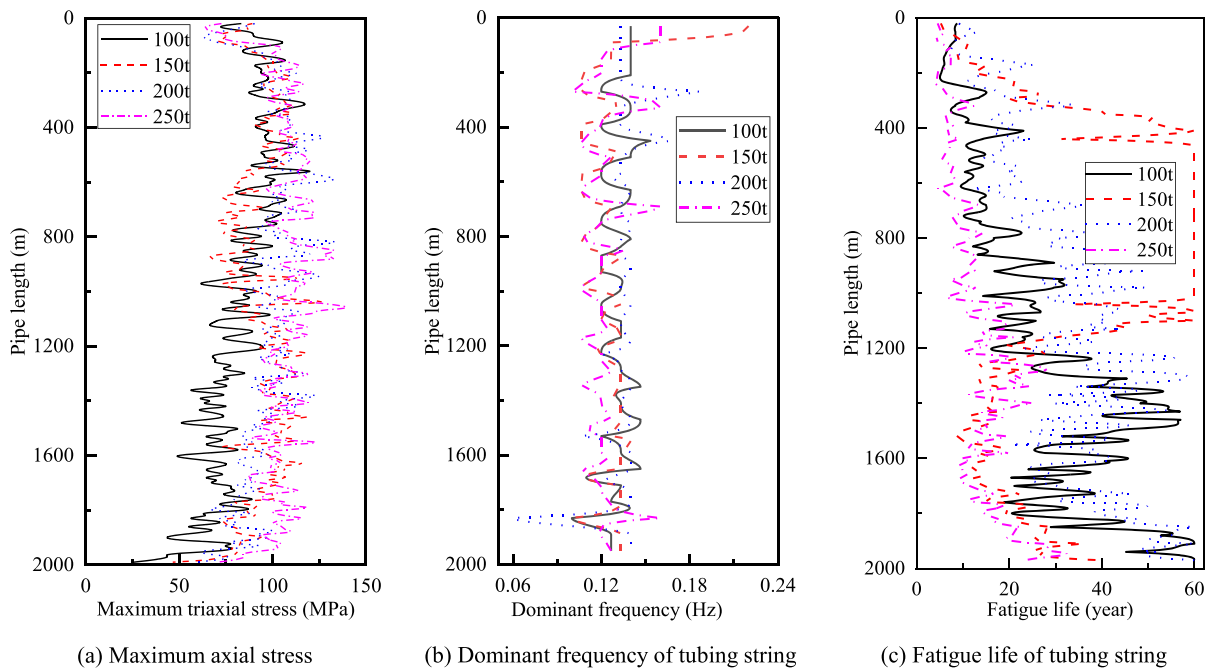


Fig. 17 Fatigue damage analysis data of lifting pipe under different buffer station masses

meeting the mining requirements, the model in this paper can be used to evaluate the safety of the entire pipe system, so as to improve the service life of the on-site pipe system.

Figure 15 shows the displacement in IL direction of lifting pipe at different positions under different buffer station masses. As can be seen that, with the increase in the buffer station mass, the IL vibration displacement at the upper part of the pipe does not change significantly (Fig. 15a and b), but the vibration displacement at the middle and lower part of the lifting pipe decreases significantly (Fig. 15c and d). The main reason is that with the increase in the buffer station mass, the unit mass matrix of the system increases, while the IL external excitation load matrix does not change, resulting in the IL displacement decreases. Since the buffer station mass is located at the lower end of the lifting pipe, the impact on the upper pipe is small. At the same time, it is found that with the increase in the buffer station mass, the vibration frequency of the lifting pipe increases along the IL direction, and complex local small vibration occurs.

Figure 16 shows the displacement in CF direction of lifting pipe at different positions under different buffer station masses. As can be seen that, with the

increase in the buffer station mass, the CF vibration displacement at the upper part of the pipe does not change significantly (Fig. 16a and b), but the vibration displacement at the middle and lower part of the lifting pipe decreases significantly (Fig. 16c and d). The reason is that as the mass of the buffer station increases, the entire lifting pipe is straightened, and under the same external flow, the lateral vibration frequency of the riser also increases. At the same time, the vortex shedding frequency of the external flow field is closer to the vibration frequency of the riser, ultimately leading to a change in the vibration amplitude of the lifting pipe.

Figure 17 shows the fatigue damage analysis data of lifting pipe under different buffer station masses including maximum axial stress, dominant frequency and fatigue life of the lifting pipe. As can be seen that, with the increase in the buffer station mass, the maximum triaxial stress of the lifting pipe shows an increasing trend. When the buffer station mass changes from 100 to 150 t, the maximum triaxial stress changes more obviously. When the buffer station mass changes from 150 to 250 t, the maximum triaxial stress increases less obviously (as shown in Fig. 17a). The main reason is that the increase in the buffer station mass will affect the axial stress and

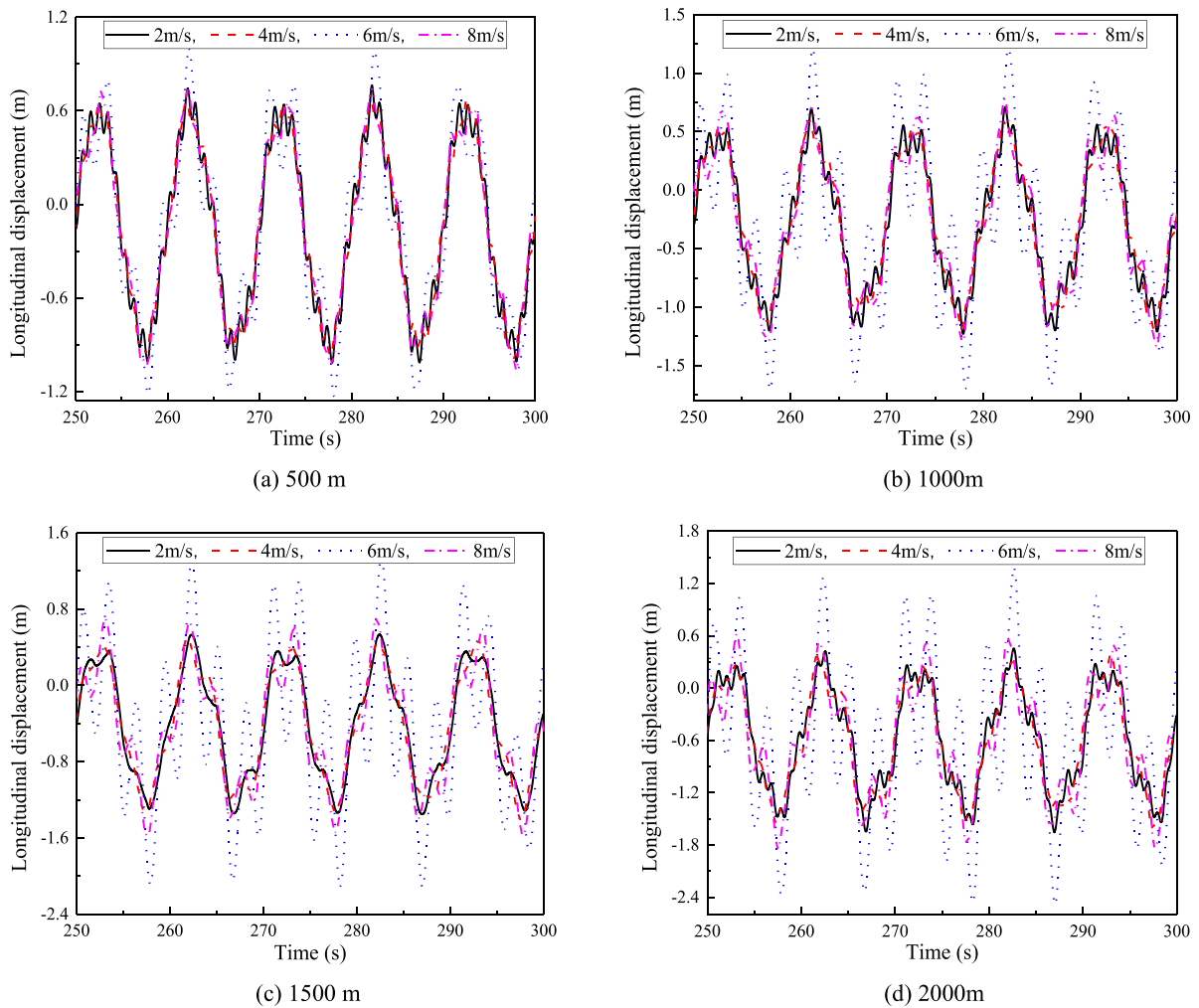


Fig. 18 Longitudinal displacement of lifting pipe at different positions under different internal flow velocities

bending stress of the lifting pipe (both jointly determine the triaxial stress of the pipe). With the increase in the buffer station mass to a certain extent, the lateral vibration of the pipe will be seriously reduced, resulting in the decrease in its bending stress, which will lead to a lower increase in the riser. Meanwhile, it is found that with the increase in the buffer station mass, the main frequency of the riser vibration shows a decreasing trend, which indicates that the increase in the buffer station mass can effectively reduce the vibration frequency of the lifting pipe (as shown in Fig. 17b). Figure 17c shows that with the increase in the buffer station mass, the fatigue life of the lifting pipe tends to decrease first and then increase. The main reason is that the increase in the buffer station mass not

only affects the triaxial stress of the lifting pipe, but also affects the main frequency of the lifting pipe, and shows the opposite trend of variation. At the early stage of the increase in the buffer station mass, the increase in triaxial stress leads to the decrease in the fatigue life of the lifting pipe. When the buffer station mass increases to a certain value, the decrease in the main frequency of the pipe determines the decrease in its fatigue life, and finally makes the fatigue life of the pipe increase first and then decrease. It can be seen that there is an optimal buffer station mass configuration parameter on the site, which is related to the riser structure, ocean flow velocity and internal flow velocity. Therefore, the analysis model established in this paper can be used to determine the buffer

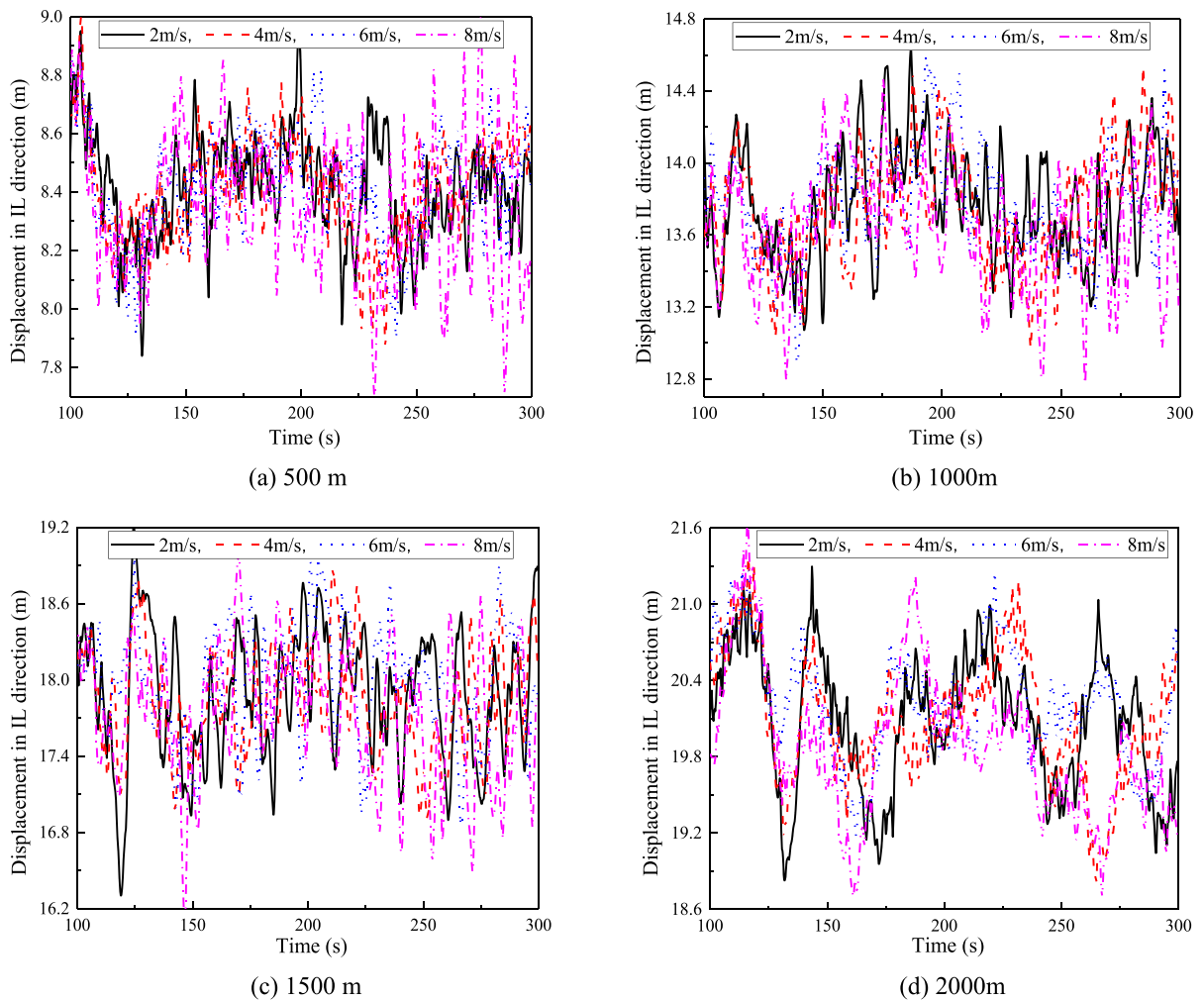


Fig. 19 Displacement in IL direction of lifting pipe at different positions under different internal flow velocities

station mass parameters in field operation, so as to improve the service life of the riser.

3.4 Influence of internal flow velocity

As an important parameter affecting the mining efficiency, the greater the internal flow rate, the greater the lifting efficiency. The site designer hopes to configure a high-flow rate to improve the mining efficiency. However, the higher the flow rate will have an impact on the safety of the pipe. Therefore, in this work, the effects of different internal flow rates on the response and fatigue life of the lifting pipe are investigated, and the corresponding design methods are proposed. The internal flow velocity is set as 2, 4, 6 and 8 m/s, respectively. And keeping outflow velocity

and the buffer station mass unchanged, which are, respectively, set as 1.35 m/s and 150 t. The curves of displacement in three directions, maximum axial stress, dominant frequency and fatigue life corresponding to different positions of lifting pipe, are obtained, as shown in Figs. 18, 19, 20 and 21.

Figure 18 shows that the change of wave parameters has little influence on the in-line flow offset of the lifting pipe, but has a significant influence on the root-mean-square stress. With the increase in the internal flow velocity, the longitudinal vibration displacement of the pipe does not change significantly (for example, when the flow rate is 2, 4 and 8 m/s, as shown in Fig. 18a and b), and there is a slight increase. However, when the internal flow rate is 6 m/s, the longitudinal displacement of the riser changes

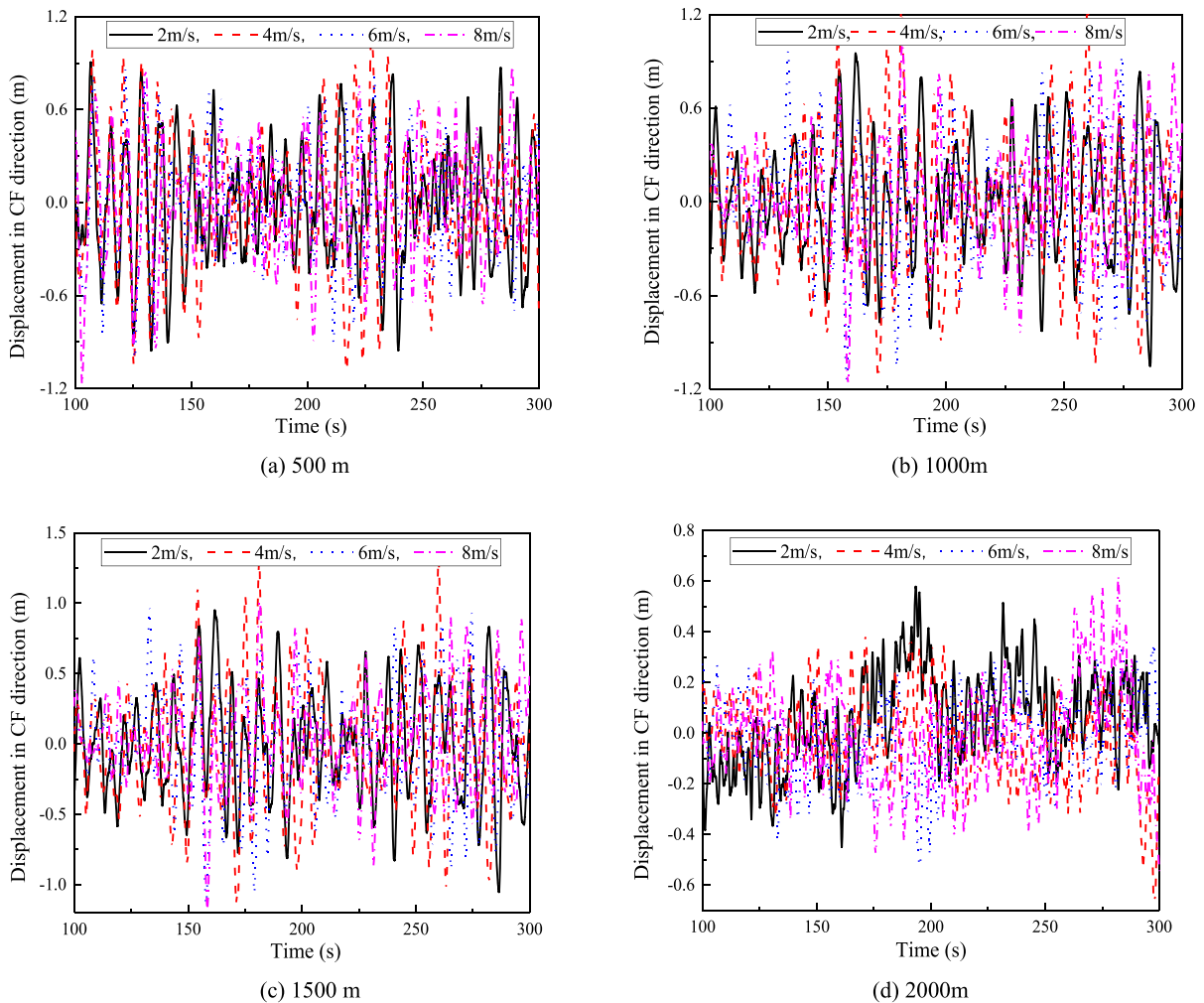


Fig. 20 Displacement in CF direction of lifting pipe at different positions under different internal flow velocities

significantly (Fig. 18c and d). The main reason is that the increase in the internal flow rate mainly affects the quality of the internal flow field unit, and the Coriolis force and centrifugal force of the pipe mainly affect the transverse vibration of the pipe. It has little effect on the longitudinal force of the pipe. However, when the internal flow rate is 6 m/s, the main reason for the large change is that the main frequency of the riser system is close to the external excitation frequency, resulting in the longitudinal resonance of the pipe.

It can be observed from Figs. 19 and 20, with the increase in the internal flow velocity, the lateral vibration of the riser (including the CF direction and the IL direction) has a significant increase trend, and a more complex nonlinear vibration form appears. The main reason is that the Coriolis force and centrifugal

force generated by the internal flow field on the pipe increase with the increase in the internal flow velocity, resulting in the more obvious impact of the internal flow on the pipe. It is also found that the larger the internal flow velocity, the greater the increase in the vibration amplitude of the pipe, and the more obvious the change of the position of the lower part of the pipe. The main reason is that the lower end of the pipe is the free end, and no effective external constraint is formed. With the increase in the internal flow field force, the effect on the vibration amplitude of the lifting pipe is more obvious. Therefore, when large flow velocity operation is adopted on-site, it is necessary pay attention to the lateral vibration of riser, especially the vibration state at the lower part of the pipe.

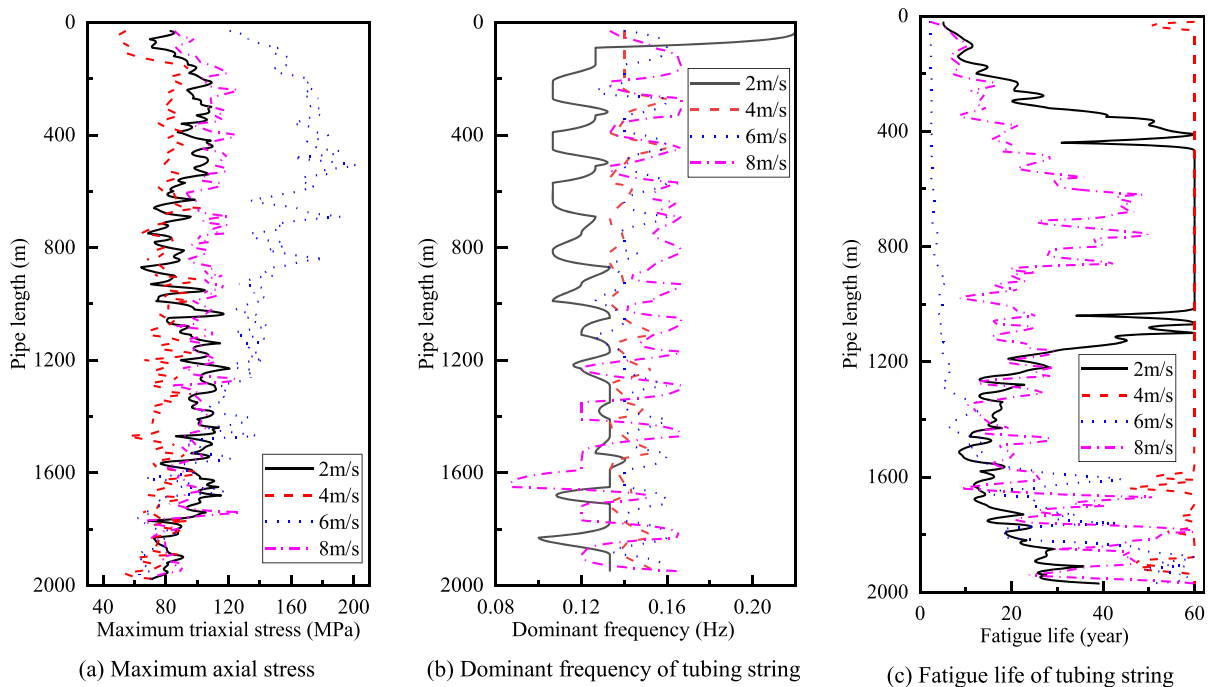


Fig. 21 Fatigue damage analysis data of lifting pipe under different internal flow velocities

Figure 21 shows the fatigue damage analysis data of lifting pipe under different internal flow velocities including maximum axial stress, dominant frequency and fatigue life of the lifting pipe. With the increase in lifting flow rate, the maximum triaxial stress of the riser increases first and then decreases (as shown in Fig. 21a). When the flow rate changes from 4 to 6 m/s, the triaxial stress increases significantly. The main reason is that the increase in the internal flow rate mainly affects the quality of the internal flow field unit, and the Coriolis force and centrifugal force of the pipe mainly affect the transverse vibration of the pipe. It has little effect on the longitudinal force of the pipe. However, when the internal flow rate is 6 m/s, the main reason for the large change is that the main frequency of the riser system is close to the external excitation frequency, resulting in the longitudinal resonance of the pipe. Meanwhile, it was found that with the increase in the internal flow rate, the triaxial stress of the pipe at the middle and upper positions was most affected, and the triaxial stress of the riser at the lower positions was less affected. Therefore, when it is necessary to configure a higher lifting flow rate during field operation, the fatigue damage of the pipe at the upper end should be paid attention to. Moreover, with

the increase in the internal flow rate, the dominant frequency of the pipe tends to increase (as shown in Fig. 21b). When setting the internal flow rate, it is necessary to combine the natural frequency of the pipe system so that its vibration frequency is far away from the natural frequency of the pipe system, which can effectively reduce the vibration amplitude of the lifting pipe. It can be observed from Fig. 21c, with the increase in the lifting flow rate, the fatigue life of the lifting pipe tends to increase first and then decrease. Among them, when the flow rate is 6 m/s, the fatigue life of the lifting pipe is the lowest, about 3 years, which seriously affects the field operation of the lifting pipe. Therefore, when determining to configure the lifting flow rate on-site, it is necessary to use the model established in this paper to analyze whether it is in a dangerous state. If it does not meet the site requirements, other parameters can be set, to improve the fatigue life of the lifting pipe.

4 Conclusions

- (1) In this work, firstly, the three-dimensional (3D) multi-field coupling nonlinear vibration model

of lifting pipe is established using the micro-finite method, energy method and Hamilton variational principle, which can accurately determine the alternating stress of deep-ocean lifting pipe. Secondly, the nonlinear fatigue damage prediction method of lifting pipe based on load interaction effect and residual strength attenuation degradation is established using Corten–Dolan cumulative damage method, which can accurately determine the fatigue life of deep-ocean lifting pipe. Finally, by comparing with the experimental results, it is found that the fatigue prediction model established in this work has the highest calculation accuracy, which effectively verifies the correctness and effectiveness of the fatigue wear prediction model established in this manuscript.

- (2) Using the proposed nonlinear fatigue damage analysis methodology of deep-ocean lifting pipe, the nonlinear vibration characteristics of lifting pipe are explored. It can be seen that, with the increase in the towing speed, the vibration state of the lifting pipe transits from the chaotic motion of the phase trajectory to the toroidal motion of the phase trajectory. With the increase in the lifting speed, the toroidal distribution is more uniform. As the vibration of vertically and horizontally coupled nonlinear lifting hard pipe is highly nonlinear, when the external flow and the internal lifting flow velocity are high, its phase trajectory presents a torus, but the vibration is always chaotic, and it is difficult to form periodic or quasi-periodic motion.
- (3) The influence of outflow velocity, buffer station masses and internal flow velocity on the fatigue life of lifting pipe is analyzed. It is found that, firstly, with the increase in the outflow velocity, the fatigue life of the pipe tends to decrease first and then increase, and an external flow rate with the maximum fatigue life appears. However, in real operation, the external flow rate cannot be controlled. Therefore, according to a certain external flow rate, the optimal structure setting can be evaluated by changing the structure of the riser, and the analysis method established in this paper to improve the service life of the lifting pipe. Secondly, with the increase in the buffer station mass, the fatigue life of the lifting pipe tends to decrease first and then increase.

There is an optimal buffer station mass configuration parameter on the site, which is related to the riser structure, ocean flow velocity, internal flow velocity and can be determined by the analysis methodology. Thirdly, with the increase in the lifting flow rate, the fatigue life of the lifting pipe tends to increase first and then decrease. Therefore, when determining to configure the lifting flow rate on-site, it is necessary to use the model established in this paper to analyze whether it is in a dangerous state. If it does not meet the site requirements, other parameters can be set, to improve the fatigue life of the lifting pipe.

Funding This work was partially supported by the National Natural Science Foundation of China (Grant Nos. 52105125 and 11972145), Fellowship of China Postdoctoral Science Foundation (Grant Nos. 2021TQ0273 and 2022M712643), Natural Science Foundation Project of Sichuan Province (Grant No. 2022NSFSC1922), Key Laboratory of Gas Hydrate, Guangzhou Institute of Energy Conversion, Chinese Academy of Sciences (No. E229kf15) and Innovative Research Groups of Natural Science Foundation of Hebei Province (A2020202002).

Data availability The data used to support the findings of this study are included within the article.

Declarations

Conflict of interest The authors declare that they have no known competing financial interests or personal relationships that could have appeared to influence the work reported in this paper.

References

1. Hannington, M., Petersen, S., Krättschell, A.: Subsea mining moves closer to shore. *Nat. Geosci.* **10**(3), 158–159 (2017)
2. Yamazaki, T.: Past, present and future of deep-sea mining. *Shigen Sozai* **131**(12), 592–596 (2016)
3. Yang, J.M., Liu, L., Lyu, H.N., Lin, Z.Q.: Deep-sea mining equipment in China: current status and prospect. *Strateg. Study CAE* **22**(6), 1–9 (2020)
4. Verichev, S., Metrikine, A., Plat, R., Hendrikse, H.: Dynamics of the vertical hydraulic transport system for deep sea mining. In: *Proceedings of the ASME 2011 30th International Conference on Ocean, Offshore and Arctic Engineering*, vol. 4, pp. 461–468. Rotterdam, The Netherlands (2011)
5. Govardan, R., Williamson, C.: Modes of vortex formation and frequency response of a freely vibrating cylinder. *J. Fluid Mech.* **420**(420), 85–130 (2000)

6. Bearman, P.W.: Vortex shedding from oscillating bluff bodies. *Annu. Rev. Fluid Mech.* **16**(1), 195–222 (2003)
7. Dahl, J.M., Hover, F.S., Triantafyllou, M.S., Oakley, O.H.: Dual resonance in vortex-induced vibrations at subcritical and supercritical Reynolds numbers. *J. Fluid Mech.* **643**(3), 395–424 (2010)
8. Facchinetti, M.L., Langre, E.D., Biolley, F.: Coupling of structure and wake oscillators in vortex-induced vibrations. *J. Fluids Struct.* **19**(2), 123–140 (2004)
9. Huera-Huarte, F.J., Bangash, Z.A., González, L.M.: Towing tank experiments on the vortex-induced vibrations of low mass ratio long flexible cylinders. *J. Fluids Struct.* **48**, 81–92 (2014)
10. Gao, Y., Fu, S., Wang, J., Song, L., Chen, Y.: Experimental study of the effects of surface roughness on the vortex-induced vibration response of a flexible cylinder. *Ocean Eng.* **103**(1), 40–54 (2015)
11. Bourguet, R., Karniadakis, G.E., Triantafyllou, M.S.: Distributed lock-in drives broadband vortex-induced vibrations of a long flexible cylinder in shear flow. *J. Fluid Mech.* **717**(1), 361–375 (2013)
12. Mao, L., Zeng, S., Liu, Q., Wang, G., He, Y.: Dynamical mechanics behavior and safety analysis of deep water riser considering the normal drilling condition and hang-off condition. *Ocean Eng.* **199**, 106996 (2020)
13. Mathelin, L., Langre, E.: Vortex-induced vibrations and waves under shear flow with a wake oscillator model. *Eur. J. Mech. B. Fluids* **24**(4), 478–490 (2005)
14. Xu, J., Wang, D., Huang, H., Duan, M., Gu, J., An, C.: A vortex-induced vibration model for the fatigue analysis of a marine drilling riser. *Ships Offshore Struct.* **12**(sup1), S280–S287 (2017)
15. He, F., Dai, H., Huang, Z., Wang, L.: Nonlinear dynamics of a fluid-conveying pipe under the combined action of cross-flow and top-end excitations. *Appl. Ocean Res.* **62**, 199–209 (2017)
16. Jauvtis, N., Williamson, C.H.K.: Vortex-induced vibration of a cylinder with two degrees of freedom. *J. Fluids Struct.* **17**(7), 1035–1042 (2003)
17. Gu, J., Yang, C., Zhu, X.Y., Wu, J.: Influences of mass ratio on vortex induced vibration characteristics of a circular cylinder. *J. Vib. Shock* **35**(4), 134–140 (2016)
18. Martins, F.A.C., Avila, J.P.J.: Effects of the Reynolds number and structural damping on vortex-induced vibrations of elastically-mounted rigid cylinder. *Int. J. Mech. Sci.* **156**, 235–249 (2019)
19. Gao, G., Cui, Y., Qiu, X., Shu, Q.: Parameter influencing analysis of vortex-induced vibration response of deep sea top tensioned riser. *Shipbuild. Eng.* **41**(2), 101–107 (2019)
20. Liu, J., Zhao, H., Liu, Q., He, Y., Wang, G., Wang, C.: Dynamic behavior of a deepwater hard suspension riser under emergency evacuation conditions. *Ocean Eng.* **150**, 138–151 (2018)
21. Liu, J., Guo, X., Liu, Q., Wang, G., He, Y., Li, J.: Vortex induced vibration response characteristics of marine riser considering the in-line and cross-flow coupling effect. *Acta Pet. Sin.* **40**(10), 1270–1280 (2019)
22. Guo, X.Q., Li, X., He, Y.F., Liu, J., Wang, G.R., Mao, L.J., Wang, J.X.: Investigation on three-dimensional vibration model and response characteristics of deep-water riser-test pipe system. *Commun. Nonlinear Sci. Numer. Simul.* **109**, 106296 (2022)
23. Miwa, S., Liu, Y., Hibiki, T., Ishii, M.: Study of unsteady gas-liquid two-phase flow induced force fluctuation (part I: evaluation and modeling of two-phase flow induced force fluctuation). *Trans. JSME* **80**(809), 1–11 (2014)
24. Shen, P.C., Liu, Q., Qi, H.H., Huang, X., Liu, J., Chen, G.: Study on flow-induced vibration damping simulation of heat exchanger tube in non-uniform two-phase flow. *Nuclear Power Eng.* **41**(06), 116–120 (2020)
25. Liang, W., Luo, M.: Numerical simulation of vortex-induced vibration of a marine riser with a multiphase internal flow considering hydrate phase transition. *Ocean Eng.* **216**, 107758 (2020)
26. Zhu, H., Gao, Y., Zhao, H.: Experimental investigation of slug flow-induced vibration of a flexible riser. *Ocean Eng.* **189**, 106370 (2019)
27. Liu, L.: Research on dynamic performance of solid-liquid two-phase flow in hydraulic transport in deep sea mining. Shanghai Jiao Tong University (2019)
28. Duan, J.L., Zhou, J.F., You, Y.X., Wang, X.: Time-domain analysis of vortex-induced vibration of a flexible mining riser transporting flow with various velocities and densities. *Ocean Eng.* **220**, 108427 (2021)
29. Li, Y., Liao, K.F., Lu, F., Liu, S.J.: Dynamic analysis of 1000 m deep-ocean lifting pipes considering fluid-structure interaction. *J. Water Resour. Water Eng.* **28**(1), 163–168 (2017)
30. Thorsen, M.J., Challabotla, N.R., Sævik, S., Nydal, O.J.: A numerical study on vortex-induced vibrations and the effect of slurry density variations on fatigue of ocean mining risers. *Ocean Eng.* **174**, 1–13 (2019)
31. Zhou, Z., Wang, Z., Lu, H., Xia, Y.: Dynamic characteristics analysis for fluid-solid coupling of vertical lifting pipe in transporting coarse particles[J]. *Appl. Mech. Mater.* **160**, 35–41 (2012)
32. Liu, Y., Chen, L.Y.: Influence of vortex induced vibration on the liquid-solid two-phase flow in pipeline. *J. Shanghai Jiao Tong Univ.* **51**(4), 485–489 (2017)
33. Yoon C., Park Y.C., Lee D.K., Kwon K.S.: Behavior of deep sea mining pipe and its effect on internal flow. In: Proceedings of the 5th ISOPE Ocean Mining Symposium, pp. 76–82. ISOPE, Tsukuba, Japan (2003)
34. Monsalve-Giraldo, J.S., Videiro, P.M., Mendes de Sousa, F.J., dos Santos, C.M.P.M., Sagrilo, L.V.S.: Parametric interpolation method for probabilistic fatigue analysis of steel risers. *Appl. Ocean Res.* **90**, 101838 (2019)
35. Chen, R.F., Low, Y.M.: Efficient long-term fatigue analysis of deepwater risers in the time domain including wave directionality. *Mar. Struct.* **78**, 103002 (2021)
36. Liu, J., Du, Z.G., Guo, X.Q., Dai, L.M., Huang, L., Li, X.: VIV fracture investigation into 3D marine riser with a circumferential outside surface crack. *Shock Vib.* **2021**, 1–13 (2021)
37. Fu, P., Leira, B.J., Myrhaug, D.: Reliability analysis of wake-induced collision of flexible risers. *Appl. Ocean Res.* **62**, 49–56 (2017)
38. Lekkala, M.R., Mohamed, L., Hafiz, M.F.U., Kim, D.K.: A practical technique for hydrodynamic coefficients modification in SHEAR7 for fatigue assessment of riser buoyancy modules under vortex-induced vibration. *Ocean Eng.* **217**, 107760 (2020)

39. Jeong, H., Jang, B.S., Kim, J.D., Park, G., Choi, J.: A study on effects of slug flow on dynamic response and fatigue damage of risers. *Ocean Eng.* **217**, 107965 (2020)
40. Ruan, W.D., Shi, J.C., Sun, B., Qi, K.F.: Study on fatigue damage optimization mechanism of deepwater lazy wave risers based on multiple waveform serial arrangement. *Ocean Eng.* **228**, 108926 (2021)
41. Gao, Z.G., Efthymiou, M., Cheng, L., Zhou, T.M., Minguez, M., Zhao, W.H.: Fatigue analysis of water intake risers: Hydrodynamic damping effect and a hybrid frequency-time domain method. *Mar. Struct.* **75**, 102869 (2021)
42. Liu, J., Zeng, L.L., Guo, X.Q., Wang, P.C., Dai, L.M.: Multi-field coupling nonlinear vibration characteristics of hydraulic lifting pipe in deep-ocean mining. *Appl. Ocean Res.* **120**, 103074 (2022)
43. Shen, W.J.: Study on the nonlinear stochastic dynamic response characteristics of a Truss Spar. Tianjin University, Tianjin (2012)
44. Longuet-Higgins, M.S.: The effect of non-linearities on statistical distributions in the theory of sea waves. *J. Fluid Mech.* **17**(03), 459–480 (1963)
45. Gao, H.Y.: Research on fatigue life prediction methods of welded joints under complex stress states. University of Electronic Science and Technology of China, Chengdu (2016)
46. Xue, Q.W., Du, X.Y., Wang, S.W.: An improved fatigue life prediction model based on loading sequence. *China Railw. Sci.* **40**(1), 88–93 (2019)
47. Carvalho André, L.M., Martins Juliana, P., Voorlwad Herman, J.C.: Fatigue damage accumulation in aluminum 7050–T7451 alloy subjected to block programs loading under step-down sequence. *Procedia Eng.* **2**(1), 2037–2043 (2010)
48. Xiao, L.J., Zhang, W.M., Fang, M.: Study of nonlinear dynamic characteristics on deep ocean lifting pipe. *J. China Coal Soc.* **27**(4), 417–421 (2002)
49. Zhou, S., Liu, Q., Jiang, W., Mao, L., Yang, X., Liu, Z., Wang, G., Huang, X., Shi, X.: The discovery of “one third effect” for deep water drilling riser: based on the theoretical and experimental study of the deformation characteristics of deep water drilling riser by ocean currents. *China Offshore Oil Gas* **25**(6), 1–7 (2013)

Publisher's Note Springer Nature remains neutral with regard to jurisdictional claims in published maps and institutional affiliations.

Springer Nature or its licensor (e.g. a society or other partner) holds exclusive rights to this article under a publishing agreement with the author(s) or other rightsholder(s); author self-archiving of the accepted manuscript version of this article is solely governed by the terms of such publishing agreement and applicable law.